UAV Positioning and Power Control for Two-Way Wireless Relaying

Lei Li, Tsung-Hui Chang, *Senior Member, IEEE*, and Shu Cai, *Member, IEEE*

***Abstract*— This paper considers an unmanned-aerial-vehicle-enabled (UAV-enabled) wireless network where a relay UAV is used for two-way communications between a ground base station (BS) and a set of distant user equipment (UE). The UAV adopts the amplify-and-forward strategy for two-way relaying over orthogonal frequency bands. The UAV positioning and the transmission powers of all nodes are jointly designed to maximize the sum rate of both uplink and downlink subject to transmission power constraints and the signal-to-noise ratio constraint on the UAV control channel. The formulated joint positioning and power control (JPPC) problem has an intricate expression of the sum rate due to two-way transmissions and is difficult to solve in general. We propose a novel concave surrogate function for the sum rate and employ the successive convex approximation (SCA) technique for obtaining a high-quality approximate solution. We show that the proposed surrogate function has a small curvature and enables a fast convergence of SCA. Furthermore, we develop a computationally efficient JPPC algorithm by applying the fast iterative shrinkage-thresholding algorithm (FISTA) type accelerated gradient projection (AGP) algorithm to solve the SCA problem as well as one of the projection subproblems, resulting in a double-loop AGP method. Simulation results show that the proposed JPPC algorithms are not only computationally efficient but also greatly outperform the heuristic approaches.**

***Index Terms*— UAV, two-way relaying, joint positioning and power control, non-convex optimization, successive convex optimization.**

I. Introduction

RECENTLY, deploying unmanned aerial vehicles (UAVs) in wireless communication networks for coverage and throughput enhancement has attracted significant attention from both the industry and academia [1]–[4]. The swift mobility of UAV enables fast deployment and establishment of communications in emergency situations such as for rescue after hurricane or earthquake. The lower cost of UAV than the traditional communication infrastructure also makes UAV a cost-effective option for the network coverage and throughput enhancement in coverage-limited zones like the rural or mountainous areas. Besides, UAVs in general have better air-to-ground (A2G) channels due to a high probability of line of sight (LoS) link with ground users [5]. Therefore, the UAV has been considered for being an aerial base station (BS) [6]–[11], wireless relay [12]–[17], and for networking [18], [19] as well as for data collection and dissemination in wireless sensor networks [20]–[24]. Several industrial projects that leverage the UAV for enhanced wireless communications, like the Facebook's laser drone test [25] and Qualcomm's drone communication plan [4], are also proposed.

A. Related Works

There are still many technical challenges to overcome in order to harvest the benefits of UAV-enabled wireless communications [2], [3]. Specifically, the air-to-ground (A2G) channel is different from the existing ground-to-ground channel, and is highly dependent on the position of UAV. In addition, due to limited battery energy, joint positioning/flying trajectory design and transmission power control are critical to achieve high spectral efficiency and energy efficiency in UAV-enabled communication systems; see [3] for a general framework for the co-design problem of UAV trajectory and communication. In particular, reference [6] derived a fix-wing UAV propulsion energy consumption model and studied the joint UAV trajectory and transmission power control problem for maximizing the system energy efficiency. By deploying the UAV as an aerial BS, reference [7] studied the trajectory and power control problem for maximizing the minimum downlink rate of ground users over orthogonal channels. By assuming that the aerial BS is equipped with a directional antenna of adjustable beamwidth, reference [8] considered joint optimization of the UAV flying altitude and beamwidth for throughput maximization in multicast, broadcast and uplink scenarios, respectively. Reference [9] considered the placement of a minimum number UAV-mounted BSs for providing required quality of service for the ground users, while [10] studied the joint scheduling, flying trajectory and power control of multiple UAV-mounted BSs for maximizing the minimum rate of served ground users. Unlike [9], [10], by modeling

Manuscript received April 10, 2019; revised August 31, 2019; accepted October 23, 2019. Date of publication November 5, 2019; date of current version February 11, 2020. The work of T.-H. Chang was supported in part by the Natural Science Foundation of China under Grant 61571385 and Grant 61731018 and in part by the Shenzhen Fundamental Research Fund under Grant ZDSYS201707251409055 and Grant KQTD2015033114415450. The work of S. Cai was supported in part by the Natural Science Foundation of China under Grant U1805262. The associate editor coordinating the review of this article and approving it for publication was Y. Chen. *(Corresponding author: Tsung-Hui Chang.)*

L. Li was with the School of Science and Engineering, The Chinese University of Hong Kong, Shenzhen 518172, China. He is now with The Bradley Department of Electrical and Computer Engineering, Virginia Polytechnic Institute and State University, Blacksburg, VA 24061 USA (e-mail: lei.ap@outlook.com).

T.-H. Chang is with the School of Science and Engineering, The Chinese University of Hong Kong, Shenzhen 518172, China, and also with the Shenzhen Research Institute of Big Data, 518172, China (e-mail: tsunghui.chang@ieee.org).

S. Cai is with the Jiangsu Key Laboratory of Wireless Communications, Nanjing University of Posts and Telecommunications, Nanjing 210003, China (e-mail: caishu@njupt.edu.cn).

Color versions of one or more of the figures in this article are available online at http://ieeexplore.ieee.org.

Digital Object Identifier 10.1109/TWC.2019.2950301

the positions of the UAVs as a 3-dimensional Poisson point process, the work of [11] considered the spectrum sharing problem between the cellular network and drone small cells, and investigated the deployment density of UAVs to maximize the outage-constrained throughput. While most of the aforementioned works have assumed deterministic LoS links, the work [26] has studied the optimal flying altitude of a UAV for coverage maximization under a probabilistic LoS channel model [27].

When the UAV is deployed as a wireless relay, the position and flying trajectory design are also of great importance [12]. References [28] and [29] considered an amplify-and-forward (AF) UAV relay for extending the service of a ground BS, and studied the joint power allocation and UAV positioning problem for sum rate and minimum rate maximization, respectively. The work [13] considered an uplink relaying system and optimized the flying heading of the UAV for maximizing an ergodic transmission rate. In [14], a decode-and-forward relay system is considered, and the UAV flying trajectory and transmission power are jointly optimized for maximizing the throughput between the ground BS and user equipment (UE). In [16], the authors considered the UAV positioning problem in a relay system by incorporating the local topological information, where the UAV is aimed to be deployed in a position that can enjoy LoS links. The work [15] considered an uplink multi-UAV relaying system under the LoS channels with random phase. The UAV positions and UE transmission powers are jointly optimized to maximize the minimum ergodic throughput of ground UEs. Reference [17] considered the use of a relay UAV for communicating with another observation UAV and studied the optimal positioning of the relay UAV for throughput maximization. The works [18] and [19] considered the deployment of multiple relay UAVs to form an ad-hoc network and achieve long distance communications, respectively.

B. Contributions

In this paper, we consider a wireless AF relay network where the UAV is used to extend the service of a BS for a set of distant ground UEs, as shown in Fig. 1. Different from the aforementioned works [28], [29] where either uplink or downlink transmission is considered, we consider the two-way communications between the BS and ground UEs. Besides, unlike [7], [13] which consider only one-hop communication between the UEs and UAV, we consider the two-hop communications where the relay UAV amplifies and forwards the signals from one side to the other.

We assume the LoS channels and aim to optimize the UAV position and transmission powers of the BS, UEs and the UAV jointly, for maximizing the sum rate of the two-way communication links. Except for the maximum transmission power constraints, we also consider the quality of service (QoS) constraint on the control link between the BS and the relay UAV. In practice, the control link is used for control and command signaling between the relay UAV and the BS, and is essential to the UAV motion control. The formulated joint UAV positioning and power control (JPPC) problem has a complicated non-concave sum rate function and is difficult to solve in general. The main contributions are summarized as below.

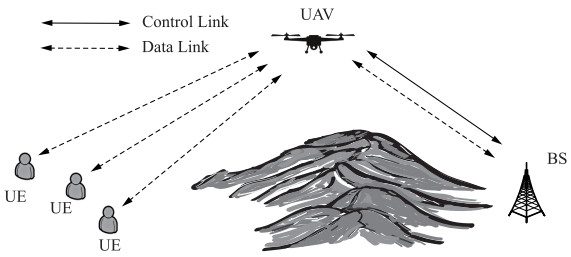

Fig. 1. UAV-enabled two-way relay communications.

1) We first consider a simple scenario with only one UE [12], and present a semi-analytical solution to the JPPC problem. It is shown that the optimal position of the relay UAV, when projected onto the x-y plane, must lie on the line segment between the BS and UE.
2) For the general case with multiple UEs, we employ the successive convex approximation (SCA) technique [30]. In SCA, one solves a surrogate convex optimization problem iteratively by replacing the non-concave objective by a concave surrogate function. Interestingly, according to [31], the curvature of the surrogate function has a direct impact on the convergence behavior of the SCA iterations. By carefully exploiting the function structure, we propose a concave surrogate function for the SCA algorithm. Moreover, we show that the proposed surrogate function has a smaller curvature than the one that is obtained by following the recent work [24], and can lead to a fast convergence of the SCA iterations. It is worthwhile to point out that SCA has also been used in many related works such as [6], [14], [28]. However, they consider SCA only for the trajectory design and employ the alternating optimization strategy to handle the joint trajectory and power control problem, which is different from the proposed algorithm which updates the UAV position and power control simultaneously.
3) The SCA algorithm requires one to globally solve the convex surrogate problem in every iteration. Since the convex surrogate problem does not admit closed-from solutions, it requires one to employ another powerful optimization method in order to solve the surrogate problem, which may not be efficient especially when the number of UEs is large. To improve the computation efficiency, we adopt a recently proposed algorithm by [32] which combines the SCA iteration with the fast iterative shrinkage-thresholding algorithm (FISTA) type accelerated gradient projection (AGP) algorithm [33]. By applying the algorithm in [32] to our JPPC problem, one of the steps involves projection onto a set of quadratic constraints. We further employ the AGP method to solve the Lagrange dual problem of the projection step. Thus, the proposed algorithm for the JPPC problem involves double loops of AGP iterations.

4) Simulation results are presented to show that the SCA algorithm using the proposed surrogate function exhibits a significantly faster convergence behavior than that using [24]. Besides, the double-loop AGP algorithm can further reduce the computation time by more than an order of magnitude. Simulation results also reveal that fact that the optimal positioning of the relay UAV is not trivial since the optimized solution can greatly outperform simple strategies that deploy the relay UAV on top of the BS or in a geometric center of the network.

The remainder of the paper is organized as follows. Section II presents the two-way relay system model and formulates the JPPC problem. The scenario with only one UE is studied in Section III. In Section IV, the proposed SCA algorithm and double-loop AGP algorithm are presented. The simulation results are given in Section V. Finally, conclusions are drawn in Section VI.

II. System Model and Problem Formulation

A. System Model

As illustrated in Fig. 1, we consider a UAV-enabled wireless two-way relaying communication network constituted by K UEs, one UAV and one BS. All the nodes are equipped with single antenna. It is assumed that there is no direct communication link between the UEs and the BS, and the UAV plays a role relaying the uplink signals from the UEs to the BS as well as relaying the downlink signals from the BS to the UEs. So the UAV extends the service coverage of the BS, and its flying and communication are controlled by the BS. Without loss of generality, we assume that all the UEs and the BS are located at the same ground plane. Denote by $\boldsymbol{u}_k = (x_k, y_k, 0)^T \in \mathbb{R}^3$ a three dimension (3D) location of the kth UE and by $\boldsymbol{b} = (x_b, y_b, 0)^T \in \mathbb{R}^3$ the 3D location of the BS. The UAV flies in the sky with a fixed altitude h (meters) and its 3D location is denoted by $\boldsymbol{x}_r = (x_r, y_r, h)^T \in \mathbb{R}^3$. Since the air-to-ground (A2G) channel between the UAV and BS and that between the UAV and UEs usually consist of a strong LoS link as long as the UAV flying altitude is sufficiently high (e.g., $h > 100$m) [34], we adopt this model throughout this paper.

We assume that the frequency division duplex (FDD) is used for uplink and downlink communications. The UAV works as a two-way AF relay which amplifies and forwards the uplink and downlink signals to the BS and UEs, respectively. While it is known that the decode-and-forward relay can achieve better performance in general, the AF relay has the advantage of low complexity and is favored in real-time applications [28]. Besides, the frequency division multiplexing (FDM) is used so that the communication links of different UEs are orthogonal to each other and have no cross-link interference. For the uplink transmission, i.e., the UE→UAV→BS link, we denote $p_{u,k} \geq 0$ as the transmission power of each UE k, where $k \in \mathcal{K} \triangleq \{1, \cdots, K\}$. The transmission power allocated by the UAV for relaying the uplink signals from UE k to the BS is denoted by $p^{\mathrm{U}}_{r,k} \geq 0, k \in \mathcal{K}$. For the downlink transmission, i.e., the BS→UAV→UE link, the transmission power of the BS for UE k is $p_{b,k} \geq 0, k \in \mathcal{K}$. The downlink relaying power of the UAV for UE k is denoted as $p^{\mathrm{D}}_{r,k} \geq 0, k \in \mathcal{K}$.

1) **Uplink Signal Model:** Denote $s^{\mathrm{U}}_k \sim \mathcal{CN}(0,1)$ as the Gaussian information signal sent by UE k. In the first time slot of the AF transmission, the signals received by the UAV are given by

$$y^{\mathrm{U}}_{r,k} = \sqrt{\frac{\beta p_{u,k}}{d^2_{kr}}} s^{\mathrm{U}}_k + w_r, \quad k \in \mathcal{K}, \tag{1}$$

where β is the reference channel gain at the distance 1 meter from the UE, $d_{kr} \triangleq \|\boldsymbol{x}_r - \boldsymbol{u}_k\|$ is the Euclidean distance between UE k and the UAV, and $w_r \sim \mathcal{CN}\left(0, \sigma^2\right)$ is the additive noise with zero mean and variance σ^2. In the second time slot, the UAV amplifies the received signal $y^{\mathrm{U}}_{r,k}$ and transmits it to the BS. In particular, by assuming that β, noise power and the location information of the UEs and BS are available to the UAV (thus the channel gain is known to the BS under the LoS channel model), the UAV can amplify the signal $y^{\mathrm{U}}_{r,k}$ with a gain $\sqrt{p^{\mathrm{U}}_{r,k} g^{\mathrm{U}}_{r,k}}$ where

$$g^{\mathrm{U}}_{r,k} = \frac{1}{p_{u,k}\beta d^{-2}_{kr} + \sigma^2} \tag{2}$$

is the inverse of the signal power of $y^{\mathrm{U}}_{r,k}$, and $p^{\mathrm{U}}_{r,k} > 0$ is the uplink transmission power of the UAV. Thus the received signal at the BS for UE k is given by

$$\begin{aligned} y^{\mathrm{U}}_{b,k} &= \sqrt{\frac{\beta}{d^2_{rb}}} \sqrt{p^{\mathrm{U}}_{r,k} g^{\mathrm{U}}_{r,k}}\; y^{\mathrm{U}}_{r,k} + w_b \\ &= \sqrt{\frac{\beta^2 p^{\mathrm{U}}_{r,k} p_{u,k}}{d^2_{rb} d^2_{kr}} g^{\mathrm{U}}_{r,k}} s^{\mathrm{U}}_k + \sqrt{\frac{\beta p^{\mathrm{U}}_{r,k}}{d^2_{rb}} g^{\mathrm{U}}_{r,k}} w_r + w_b, \end{aligned} \tag{3}$$

where $d_{rb} \triangleq \|\boldsymbol{x}_r - \boldsymbol{b}\|$ is the distance between the UAV and the BS and $w_b \sim \mathcal{CN}\left(0, \sigma^2\right)$ is the additive noise at the BS. By (3), the uplink signal-to-noise ratio (SNR) for the kth UE can be expressed as

$$\begin{aligned} \mathrm{SNR}^{\mathrm{U}}_k &= \frac{\beta^2 g^{\mathrm{U}}_{r,k} p^{\mathrm{U}}_{r,k} p_{u,k} d^{-2}_{rb} d^{-2}_{kr}}{\beta g^{\mathrm{U}}_{r,k} p^{\mathrm{U}}_{r,k} d^{-2}_{rb} \sigma^2 + \sigma^2} \\ &= \frac{\beta^2 p^{\mathrm{U}}_{r,k} p_{u,k} d^{-2}_{kr} d^{-2}_{rb}}{\beta p^{\mathrm{U}}_{r,k} d^{-2}_{rb} \sigma^2 + \beta p_{u,k} d^{-2}_{kr} \sigma^2 + (\sigma^2)^2} \\ &= \frac{p^{\mathrm{U}}_{r,k} p_{u,k} d^{-2}_{kr} d^{-2}_{rb} \xi}{p^{\mathrm{U}}_{r,k} d^{-2}_{rb} + p_{u,k} d^{-2}_{kr} + \xi^{-1}}, \end{aligned} \tag{4}$$

where (2) is applied to obtain the second equality and $\xi \triangleq \frac{\beta}{\sigma^2}$ is defined in the last equality.

2) **Downlink Signal Model:** In the downlink transmission, given the information signal $s^{\mathrm{D}}_k \sim \mathcal{CN}(0,1)$ for UE k sent from the BS in the first time slot, the received signal at the UAV is given by

$$y^{\mathrm{D}}_{r,k} = \sqrt{\frac{\beta p_{b,k}}{d^2_{rb}}} s^{\mathrm{D}}_k + w_r. \tag{5}$$

In the second time slot, the UAV amplifies $y^{\mathrm{D}}_{r,k}$ by the gain $\sqrt{p^{\mathrm{D}}_{r,k} g^{\mathrm{D}}_{r,k}}$, where $g^{\mathrm{D}}_{r,k} = \frac{1}{\beta p_{b,k} d^{-2}_{rb} + \sigma^2}$, and forwards it to

UE k. The received signal at UE k is given by

$$y_{b,k}^{\mathrm{U}} = \sqrt{\frac{\beta^2 p_{r,k}^{\mathrm{D}} p_{b,k}}{d_{kr}^2 d_{rb}^2} g_{r,k}^{\mathrm{D}}} s_k^{\mathrm{D}} + \sqrt{\frac{\beta p_{r,k}^{\mathrm{D}}}{d_{kr}^2} g_{r,k}^{\mathrm{D}}} w_r + w_k, \quad (6)$$

where $w_k \sim \mathcal{CN}\left(0, \sigma^2\right)$ is the additive noise at UE k. By (6), the downlink SNR for the kth UE is thus

$$\mathrm{SNR}_k^{\mathrm{D}} = \frac{p_{r,k}^{\mathrm{D}} p_{b,k} d_{rb}^{-2} d_{kr}^{-2} \xi}{p_{r,k}^{\mathrm{D}} d_{kr}^{-2} + p_{b,k} d_{rb}^{-2} + \xi^{-1}}. \quad (7)$$

Denote by $\boldsymbol{p}_r^{\mathrm{U}} \triangleq (p_{r,1}^{\mathrm{U}}, \cdots, p_{r,K}^{\mathrm{U}})^T$, $\boldsymbol{p}_r^{\mathrm{D}} \triangleq (p_{r,1}^{\mathrm{D}}, \cdots, p_{r,K}^{\mathrm{D}})^T$, $\boldsymbol{p}_b \triangleq (p_{b,1}, \cdots, p_{b,K})^T$ and $\boldsymbol{p}_u \triangleq (p_{u,1}, \cdots, p_{u,K})^T$ the vectors that collect the transmission powers of the UAV, BS and the UEs, respectively. Based on the SNR expressions in (4) and (7), the sum rate of the network is

$$R_s(\boldsymbol{x}_r, \boldsymbol{p}_b, \boldsymbol{p}_r^{\mathrm{U}}, \boldsymbol{p}_r^{\mathrm{D}}, \boldsymbol{p}_u) = \sum_{k=1}^{K} \frac{W}{2} \big(\log(1+\mathrm{SNR}_k^{\mathrm{U}}) + \log(1+\mathrm{SNR}_k^{\mathrm{D}})\big), \quad (8)$$

where $R_k^{\mathrm{U}}(\boldsymbol{x}_r, \boldsymbol{p}_r^{\mathrm{U}}, \boldsymbol{p}_u) = \frac{W}{2}\log(1+\mathrm{SNR}_k^{\mathrm{U}})$ and $R_k^{\mathrm{D}}(\boldsymbol{x}_r, \boldsymbol{p}_b, \boldsymbol{p}_r^{\mathrm{D}}) = \frac{W}{2}\log(1+\mathrm{SNR}_k^{\mathrm{D}})$ are respectively the uplink and downlink transmission rates of each UE k, in which W is the frequency bandwidth allocated for each UE. As the AF relay transmission requires two time slots, the rate is divided by 2 in (8).

3) **Control Link:** Besides the data transmission, signaling consisting of the telecommands [35] (including the command of speed, altitude and throttle from the BS to the UAV) and the telemetry (including the UAV positioning and engine information from the UAV to the BS) is critical to the UAV control. The SNR requirement of the signaling on the control link requires to be satisfied. Here, for simplicity, we assume that the control signaling in both uplink and downlink have the same SNR requirement [36]. Then, under the LoS channel model, the control link is symmetric between the BS and the UAV and both the UAV and BS use the same power for control signaling. Let us denote p_c as the transmission power for the control link. Then, the received SNR for the control link is

$$\mathrm{SNR}_c = \frac{\beta' p_c}{d_{rb}^2 \sigma^2} = \frac{\xi' p_c}{d_{rb}^2}, \quad (9)$$

where β' is the reference channel gain for the control link and $\xi' \triangleq \frac{\beta'}{\sigma^2}$.

B. Problem Formulation

Denote by P_r, P_b and $P_{u,k}$ the maximum transmission powers of the UAV, BS and each UE k. By (4), (7), (8) and (9), we consider the joint UAV positioning and power control (JPPC) problem as

$$\max_{\substack{\boldsymbol{x}_r,\ \boldsymbol{p}_b, \boldsymbol{p}_r^{\mathrm{U}}, \boldsymbol{p}_r^{\mathrm{D}}, \boldsymbol{p}_u \geq 0, \\ p_c \geq 0}} R_s(\boldsymbol{x}_r, \boldsymbol{p}_b, \boldsymbol{p}_r^{\mathrm{U}}, \boldsymbol{p}_r^{\mathrm{D}}, \boldsymbol{p}_u) \quad (10a)$$

$$\text{s.t. } \mathbf{1}^T \boldsymbol{p}_r^U + \mathbf{1}^T \boldsymbol{p}_r^{\mathrm{D}} + p_c \leq P_r, \quad (10b)$$

$$\mathbf{1}^T \boldsymbol{p}_b + p_c \leq P_b, \quad (10c)$$

$$p_{u,k} \leq P_{u,k}, k \in \mathcal{K}, \quad (10d)$$

$$\mathrm{SNR}_c \geq \gamma_c, \quad (10e)$$

where $\mathbf{1}$ is the all-one vector, and γ_c is the SNR requirement of the downlink and uplink control signaling. The constraints (10b) and (10c) are the total transmission power constraints at the UAV and the BS, respectively; (10d) constrains the maximum transmission power of each UE k. When the 3D UAV positioning design is considered, the altitude constraint of the UAV can be added in (10) as $H_{\min} \leq h \leq H_{\max}$ [24], where $H_{\min}$ is the minimum flying altitude to have the LoS channel with a high probability and $H_{\max}$ is the maximum altitude set by the airspace regulations. It can be verified that the optimal UAV altitude always satisfies $h^* = H_{\min}$ for problem (10).

Property 1: *All constraints* (10b) *to* (10e) *of problem* (10) *hold with equality at the optimum.*

Proof: It is easy to verify that $\mathrm{SNR}_k^{\mathrm{U}}$ in (4) is an increasing function of $p_{u,k}$ and $p_{r,k}^{\mathrm{U}}$, respectively; similary, $\mathrm{SNR}_k^{\mathrm{D}}$ in (7) is an increasing function of $p_{b,k}$ and $p_{r,k}^{\mathrm{D}}$, respectively. Thus, constraints (10b) to (10d) must hold with equality at the optimum. If (10e) holds with strict inequality at the optimum, then one can reduce p_c and it makes (10b) to (10d) inactive. Then, either $p_{b,k}$, $p_{r,k}^{\mathrm{U}}$ or $p_{r,k}^{\mathrm{D}}$ can be further increased to improve the sum rate. As a result, (10e) must also hold with equality at the optimum. ■

By Property 1, we obtain the optimal $p_{u,k} = P_{u,k}$, $\forall k \in \mathcal{K}$, and $p_c = (\gamma_c/\xi')\|\boldsymbol{x}_r - \boldsymbol{b}\|^2$ for problem (10). Thus, problem (10) can be simplified as

$$\max_{\boldsymbol{x}_r,\ \boldsymbol{p} \geq 0} R_s(\boldsymbol{x}_r, \boldsymbol{p}) \quad (11a)$$

$$\text{s.t. } \mathbf{1}^T \boldsymbol{p}_r^U + \mathbf{1}^T \boldsymbol{p}_r^{\mathrm{D}} + \frac{\gamma_c}{\xi'}\|\boldsymbol{x}_r - \boldsymbol{b}\|^2 \leq P_r, \quad (11b)$$

$$\mathbf{1}^T \boldsymbol{p}_b + \frac{\gamma_c}{\xi'}\|\boldsymbol{x}_r - \boldsymbol{b}\|^2 \leq P_b, \quad (11c)$$

where $\boldsymbol{p} \triangleq ((\boldsymbol{p}_r^{\mathrm{U}})^T, (\boldsymbol{p}_r^{\mathrm{D}})^T, \boldsymbol{p}_b^T)^T$, and, with a slight of abuse of notation,

$$\begin{aligned} R_s(\boldsymbol{x}_r, \boldsymbol{p}) &\triangleq \sum_{k=1}^{K} \left(R_k^{\mathrm{U}}(\boldsymbol{x}_r, p_{r,k}^{\mathrm{U}}) + R_k^{\mathrm{D}}(\boldsymbol{x}_r, p_{b.k}, p_{r,k}^{\mathrm{D}})\right), \\ R_k^{\mathrm{U}}(\boldsymbol{x}_r, p_{r,k}^{\mathrm{U}}) &= \frac{W}{2}\log\left(1 + \frac{p_{r,k}^{\mathrm{U}} P_{u,k} d_{kr}^{-2} d_{rb}^{-2} \xi}{p_{r,k}^{\mathrm{U}} d_{rb}^{-2} + P_{u,k} d_{kr}^{-2} + \xi^{-1}}\right), \\ R_k^{\mathrm{D}}(\boldsymbol{x}_r, p_{b.k}, p_{r,k}^{\mathrm{D}}) &= \frac{W}{2}\log\left(1 + \frac{p_{r,k}^{\mathrm{D}} p_{b,k} d_{rb}^{-2} d_{kr}^{-2} \xi}{p_{r,k}^{\mathrm{D}} d_{kr}^{-2} + p_{b,k} d_{rb}^{-2} + \xi^{-1}}\right). \end{aligned} \quad (12)$$

III. UAV Positioning and Power Control: Single UE Case

To gain more insights, let us first study a special instance of problem (11) with only one UE ($K = 1$). For the single UE case, problem (11) reduces to

$$\max_{\boldsymbol{x}_r,\ \boldsymbol{p} \geq 0} R_s(\boldsymbol{x}_r, \boldsymbol{p}) \quad (13a)$$

$$\text{s.t. } (p_r^U + p_r^{\mathrm{D}}) + \frac{\gamma_c}{\xi'}\|\boldsymbol{x}_r - \boldsymbol{b}\|^2 \leq P_r, \quad (13b)$$

$$p_b + \frac{\gamma_c}{\xi'}\|\boldsymbol{x}_r - \boldsymbol{b}\|^2 \leq P_b, \quad (13c)$$

where

$$R_s(\boldsymbol{x}_r,\boldsymbol{p}) = \frac{W}{2}\Bigg(\log(1+\frac{p_r^{\mathrm{U}}P_u\xi}{p_r^{\mathrm{U}}d_{ur}^2+P_u d_{rb}^2+\xi^{-1}d_{ur}^2d_{rb}^2}) +\log(1+\frac{p_r^{\mathrm{D}}p_b\xi}{p_r^{\mathrm{D}}d_{rb}^2+p_b d_{ur}^2+\xi^{-1}d_{rb}^2d_{ur}^2})\Bigg). \quad (14)$$

Here, the subscript k of all variables is removed for notation simplicity; besides, each d_{kr} is replaced by $d_{ur} = \|\boldsymbol{x}_r - \boldsymbol{u}\|$ in which $\boldsymbol{u}$ is the 3D location of the UE. It is not surprising to see that the following statement is true.

Property 2: *When projected onto the x-y plane, the optimal UAV position is on the line segment connecting the BS and the UE.*

Proof: The proof is presented in Appendix A.

By Property 2, we can write $\boldsymbol{x}_r = \boldsymbol{u} + \alpha\boldsymbol{s} + h\boldsymbol{e}_z$, where $\boldsymbol{s} = \frac{\boldsymbol{b}-\boldsymbol{u}}{\|\boldsymbol{b}-\boldsymbol{u}\|}$, $\boldsymbol{e}_z = (0,0,1)^T$ and $0 \le \alpha \le M \triangleq \|\boldsymbol{b}-\boldsymbol{u}\|$. By this expression and Property 1, we have

$$d_{ur}^2 = \|\boldsymbol{x}_r - \boldsymbol{u}\|^2 = \alpha^2 + h^2, \quad (15)$$

$$d_{rb}^2 = \|\boldsymbol{x}_r - \boldsymbol{b}\|^2 = (M-\alpha)^2 + h^2, \quad (16)$$

$$p_b = P_b - \frac{\gamma_c}{\xi'}((M-\alpha)^2 + h^2). \quad (17)$$

Thus, problem (13) is equivalent to the following problem

$$\max_{0\le\alpha\le M}\left\{\begin{array}{l}\max\limits_{p_r^{\mathrm{U}}\ge 0, p_r^{\mathrm{D}}\ge 0} R_s\left(\alpha, p_r^{\mathrm{U}}, p_r^{\mathrm{D}}\right)\\ \text{s.t. } p_r^{\mathrm{U}} + p_r^{\mathrm{D}} \le P_r - \frac{\gamma_c}{\xi'}((M-\alpha)^2+h^2)\end{array}\right\} \quad (18)$$

$$= \max_{0\le\alpha\le M} R_s^{\star}(\alpha) \quad (19)$$

where $R_s\left(\alpha, p_r^{\mathrm{U}}, p_r^{\mathrm{D}}\right)$ is obtained by substituting (15), (16) and (17) into (14), and $R_s^{\star}(\alpha)$ denotes the optimal sum rate of the inner problem in (18) with a given value of α. It is worth noting that, while problem (18) is not a convex problem, the inner problem with a given value of α is a convex problem (since $R_s\left(\alpha, p_r^{\mathrm{U}}, p_r^{\mathrm{D}}\right)$ is a concave function for $p_r^{\mathrm{U}}, p_r^{\mathrm{D}} \ge 0$), which can be efficiently solved. Therefore, one can globally solve problem (13) by searching the optimal value of $\alpha \in [0, M]$ in (19).

IV. UAV Positioning and Power Control: Multiple User Case

In this section, we study efficient algorithms to solve the UAV positioning and power control problem (11) with multiple UEs. Unlike the single user case, (11) is much more challenging to solve due to the non-concave objective function. Our aim is to develop computationally efficient algorithms for (11). Specifically, the proposed approach is based on the successive convex approximation (SCA) method [30], [31], [37], where one obtains a suboptimal solution by solving a sequence of convex surrogate problems. For our problem (11), since the constraints (11b) and (11c) are both convex, we need to find a proper concave surrogate function for the non-concave sum rate function $R_s(\boldsymbol{x}_r, \boldsymbol{p})$. Next, we propose such a concave surrogate function that is amenable for fast SCA convergence.

A. Proposed SCA Algorithm

Let us present a concave surrogate function for $R_s(\boldsymbol{x}_r, \boldsymbol{p})$ in (12). Let $(\bar{\boldsymbol{p}}_b, \bar{\boldsymbol{p}}_r^{\mathrm{D}}, \bar{\boldsymbol{p}}_r^{\mathrm{U}}, \bar{\boldsymbol{x}}_r)$ be a feasible point to problem (11). Define

$$\bar{\boldsymbol{d}}_{rb} \triangleq \bar{\boldsymbol{x}}_r - \boldsymbol{b},\ \boldsymbol{d}_{rb} \triangleq \boldsymbol{x}_r - \boldsymbol{b},$$
$$\bar{\boldsymbol{d}}_{kr} \triangleq \bar{\boldsymbol{x}}_r - \boldsymbol{u}_k,\ \boldsymbol{d}_{kr} \triangleq \boldsymbol{x}_r - \boldsymbol{u}_k,\quad k \in \mathcal{K}, \quad (20)$$

and

$$\bar{I}_k^{\mathrm{D}} \triangleq \xi^{-1}\frac{\|\bar{\boldsymbol{d}}_{rb}\|^2}{\bar{p}_{b,k}} + \xi^{-1}\frac{\|\bar{\boldsymbol{d}}_{kr}\|^2}{\bar{p}_{r,k}^{\mathrm{D}}} + \xi^{-2}\frac{\|\bar{\boldsymbol{d}}_{rb}\|^2}{\bar{p}_{b,k}}\frac{\|\bar{\boldsymbol{d}}_{kr}\|^2}{\bar{p}_{r,k}^{\mathrm{D}}}, \quad (21)$$

$$\bar{I}_k^{\mathrm{U}} \triangleq \xi^{-1}\frac{\|\bar{\boldsymbol{d}}_{kr}\|^2}{\bar{p}_{u,k}} + \xi^{-1}\frac{\|\bar{\boldsymbol{d}}_{rb}\|^2}{\bar{p}_{r,k}^{\mathrm{U}}} + \xi^{-2}\frac{\|\bar{\boldsymbol{d}}_{kr}\|^2}{\bar{p}_{u,k}}\frac{\|\bar{\boldsymbol{d}}_{rb}\|^2}{\bar{p}_{r,k}^{\mathrm{U}}}, \quad (22)$$

for all $k \in \mathcal{K}$.

Proposition 1: *The function*

$$\bar{R}_s\left(\boldsymbol{x}_r,\boldsymbol{p}\right) \triangleq \frac{W}{2}\sum_{k=1}^{K}(\bar{R}_k^{\mathrm{D}}(\boldsymbol{x}_r, p_{b,k}, p_{r,k}^{\mathrm{D}}) + \bar{R}_k^{\mathrm{U}}(\boldsymbol{x}_r, p_{r,k}^{\mathrm{U}})), \quad (23)$$

where $\bar{R}_k^{\mathrm{D}}(\boldsymbol{x}_r, p_{b,k}, p_{r,k}^{\mathrm{D}})$ *and* $\bar{R}_k^{\mathrm{U}}(\boldsymbol{x}_r, p_{r,k}^{\mathrm{U}})$ *are respectively given in* (25) *and* (26) *at the bottom of the next page, is a concave function and is a locally tight lower bound of the sum rate function* (12)*, i.e.,*

$$R_s(\bar{\boldsymbol{x}}_r, \bar{\boldsymbol{p}}) = \bar{R}_s(\bar{\boldsymbol{x}}_r, \bar{\boldsymbol{p}}),\ R_s(\boldsymbol{x}_r,\boldsymbol{p}) \ge \bar{R}_s(\boldsymbol{x}_r,\boldsymbol{p}), \quad (24)$$

for all feasible $(\boldsymbol{x}_r, \boldsymbol{p})$.

Proof: Appendix B.

As defined in (20), (21) and (22), all the constants in (25) and (26) are denoted by bar notations. By noting that $\frac{\|\mathbf{d}\|^2}{p}$ and $\left(\frac{\|\mathbf{d}\|^2}{p}\right)^2$ are convex function, one can easily verify that the surrogate functions in (25) and (26) are indeed concave and satisfy (24). By replacing the objective function of (11) by (23), we obtain the following convex optimization problem

$$\max_{\boldsymbol{x}_r,\ \boldsymbol{p}\ge 0}\ \bar{R}_s\left(\boldsymbol{x}_r,\boldsymbol{p}\right) \quad (27a)$$

$$\text{s.t. } \mathbf{1}^T\boldsymbol{p}_r^U + \mathbf{1}^T\boldsymbol{p}_r^{\mathrm{D}} + \frac{\gamma_c}{\xi'}\|\boldsymbol{x}_r - \boldsymbol{b}\|^2 \le P_r, \quad (27b)$$

$$\mathbf{1}^T\boldsymbol{p}_b + \frac{\gamma_c}{\xi'}\|\boldsymbol{x}_r - \boldsymbol{b}\|^2 \le P_b. \quad (27c)$$

The proposed SCA algorithm for solving problem (11) then iteraively solves (27) with a given feasible point $(\bar{\boldsymbol{p}}, \bar{\boldsymbol{x}}_r)$ obtained in the previous iteration, as shown in Algorithm 1. Since $\bar{R}_s\left(\boldsymbol{x}_r,\boldsymbol{p}\right)$ is a locally tight lower bound of $R_s\left(\boldsymbol{x}_r,\boldsymbol{p}\right)$ satisfying (24) and the constraint set of problem (11) is compact and convex, according to [38, Theorem 1, Proposition 1], [39] it can be shown that $(\boldsymbol{p}, \boldsymbol{x}_r)$ yielded by Algorithm 1 converges to a stationary point of problem (11) as the iteration number goes to infinity.

Remark 1: It is worthwhile to mention that, except for using the off-the-shelf convex solvers such as CVX [40] to solve (27), it would be more efficient to develop a customized algorithm. For example, because the Slater's condition holds for (27), one may consider the Lagrange dual problem of (27), i.e.,

$$\max_{\lambda\ge 0,\mu\ge 0}\left\{\min_{\boldsymbol{x}_r,\boldsymbol{p}\ge 0}\mathcal{L}_1\left(\mathbf{x}_r,\boldsymbol{p},\lambda,\mu\right)\right\}, \quad (28)$$

Algorithm 1 Proposed SCA Algorithm for Problem (11)

1: **Given** an initial point $(\boldsymbol{p}^0, \boldsymbol{x}_r^0)$ that is feasible to problem (11); Set $i = 0$.
2: **repeat**
3: Update $(\bar{\boldsymbol{p}}, \bar{\boldsymbol{x}}_r)$ by $(\boldsymbol{p}^i, \boldsymbol{x}_r^i)$.
4: Solve problem (27) and obtain the optimal solution $(\boldsymbol{p}^{i+1}, \boldsymbol{x}_r^{i+1})$.
5: $i \leftarrow i + 1$.
6: **until** $R_s(\boldsymbol{x}_r^i, \boldsymbol{p}^i) - R_s(\boldsymbol{x}_r^{i-1}, \boldsymbol{p}^{i-1}) \leq \epsilon_0$

where

$$\begin{aligned}\mathcal{L}_1\left(\mathbf{x}_r, \boldsymbol{p}, \lambda, \mu\right) = &-\bar{R}_s\left(\boldsymbol{x}_r, \boldsymbol{p}\right) \\ &+\lambda\left(\mathbf{1}^T\boldsymbol{p}_r^U + \mathbf{1}^T\boldsymbol{p}_r^{\mathrm{D}} + \frac{\gamma_c}{\xi'}\|\boldsymbol{x}_r - \boldsymbol{b}\|^2 - P_r\right) \\ &+\mu\left(\mathbf{1}^T\boldsymbol{p}_b + \frac{\gamma_c}{\xi'}\|\boldsymbol{x}_r - \boldsymbol{b}\|^2 - P_b\right) \end{aligned} \quad (29)$$

is the Lagrangian function, and $\lambda \geq 0$ and $\mu \geq 0$ are the dual variables associated with (27b) and (27c), respectively. The dual subgradient ascent (DSA) method [41] can be applied to (28) while the inner minimization problem $\min_{\boldsymbol{x}_r, \boldsymbol{p} \geq 0} \mathcal{L}(\mathbf{x}_r, \boldsymbol{p}, \lambda, \mu)$ can be solved by applying the gradient projection (GP) method [42]. Since $\mathcal{L}_1\left(\mathbf{x}_r, \boldsymbol{p}, \lambda, \mu\right)$ has a separable strucutre (it is a summation and each of the terms involves variables of either one UE or the UAV only), the GP method for the inner minimization problem can inherently be implemented in a fully parallel manner. The resultant algorithm is therefore more time efficient than the general-purpose solvers.

B. Comparison With the Surrogate Function in [24]

It is important to notice that the locally tight surrogate functions presented in Proposition 1 are simply one of the choices for SCA optimization, and a different surrgorate function may be obtained by another approach. From a theoretical point of view, as long as the surrogate function is a locally tight lower bound, i.e., satisfies (24), convergence of the SCA algorithm is guaranteed. Nevertheless, different surrogate functions may result in quite different convergence behavior. In accordance with [31, Theorem 3], the iteration complexity of the SCA algorithm is in the order of $\mathcal{O}(\frac{L^2}{\epsilon})$, where ϵ is a solution accuracy and L is the gradient Lipschitz constant of the employed surrogate function. The constant L represents the curvature and is also the spectral radius of the Hessian matrix of the surrogate function provided that it is twice differentiable.

In this subsection, we aim to demonstrate that the proposed surrogate functions in Proposition 1 is good in the sense that it has a faster convergence behavior than a surrogate function that is deduced following the idea in a recent work [24]. In particular, as we show in Appendix C, by following a similar method as in [24, Eqn. (20)], one can obtain

$$\hat{R}_s(\boldsymbol{x}_r, \boldsymbol{a}) \triangleq \frac{W}{2}\sum_{k=1}^{K}(\hat{R}_k^{\mathrm{D}}(\boldsymbol{x}_r, a_{b,k}, a_{r,k}^{\mathrm{D}}) + \hat{R}_k^{\mathrm{U}}(\boldsymbol{x}_r, a_{r,k}^{\mathrm{U}})), \quad (30)$$

as another concave and locally tight lower bound for $R_s(\boldsymbol{x}_r, \boldsymbol{p})$ in (12). Here $\hat{R}_k^{\mathrm{D}}(\boldsymbol{x}_r, a_{b,k}, a_{r,k}^{\mathrm{D}})$ and $\hat{R}_k^{\mathrm{U}}\left(\boldsymbol{x}_r, a_{r,k}^{\mathrm{U}}\right)$ are respectively given in (31) and (32) at the bottom of the next page, where $a_{b,k} = \sqrt{p_{b,k}}, a_{r,k}^{\mathrm{D}} = \sqrt{p_{r,k}^{\mathrm{D}}}$ and $a_{r,k}^{\mathrm{U}} = \sqrt{p_{r,k}^{\mathrm{U}}}$; $\bar{a}_{b,k} = \sqrt{\bar{p}_{b,k}}, \bar{a}_{r,k}^{\mathrm{D}} = \sqrt{\bar{p}_{r,k}^{\mathrm{D}}}$ and $\bar{a}_{r,k}^{\mathrm{U}} = \sqrt{\bar{p}_{r,k}^{\mathrm{U}}}$; and

$$\begin{aligned}\bar{J}_k^{\mathrm{D}} &= \xi\left(\frac{(\bar{a}_{r,k}^{\mathrm{D}})^2}{\|\boldsymbol{u}_k - \bar{\boldsymbol{x}}_r\|^2} + \frac{\bar{a}_{b,k}^2}{\|\bar{\boldsymbol{x}}_r - \boldsymbol{b}\|^2}\right), \\ \bar{J}_k^{\mathrm{U}} &= \xi\left(\frac{(\bar{a}_{r,k}^{\mathrm{U}})^2}{\|\bar{\boldsymbol{x}}_r - \boldsymbol{b}\|^2} + \frac{P_{u,k}}{\|\boldsymbol{u}_k - \bar{\boldsymbol{x}}_r\|^2}\right). \end{aligned} \quad (33)$$

Next we compare the two surrogate functions in (23) and (30) analytically and numerically. For ease of illustration,

$$\begin{aligned}\bar{R}_k^{\mathrm{D}}(\boldsymbol{x}_r, p_{b,k}, p_{r,k}^{\mathrm{D}}) \triangleq\ & \log\left(1 + \xi^{-1}\left(\frac{2\bar{\boldsymbol{d}}_{rb}^T}{\bar{p}_{b,k}}\boldsymbol{d}_{rb} - \frac{\|\bar{\boldsymbol{d}}_{rb}\|^2}{\bar{p}_{b,k}^2}p_{b,k}\right)\right) + \log\left(1 + \xi^{-1}\left(\frac{2\bar{\boldsymbol{d}}_{kr}^T}{\bar{p}_{r,k}^{\mathrm{D}}}\boldsymbol{d}_{kr} - \frac{\|\bar{\boldsymbol{d}}_{kr}\|^2}{(\bar{p}_{r,k}^{\mathrm{D}})^2}p_{r,k}^{\mathrm{D}}\right)\right) \\ &-\log(\bar{I}_k^{\mathrm{D}}) + 1 - \frac{1}{\bar{I}_k^{\mathrm{D}}\xi}\left(\frac{\|\boldsymbol{d}_{rb}\|^2}{p_{b,k}} + \frac{\|\boldsymbol{d}_{kr}\|^2}{p_{r,k}^{\mathrm{D}}}\right) - \frac{1}{2\bar{I}_k^{\mathrm{D}}\xi^2}\left(\frac{\|\boldsymbol{d}_{rb}\|^2}{p_{b,k}} + \frac{\|\boldsymbol{d}_{kr}\|^2}{p_{r,k}^{\mathrm{D}}}\right)^2 \\ &+\frac{1}{2\bar{I}_k^{\mathrm{D}}\xi^2}\Bigg[\left(\frac{4\|\bar{\boldsymbol{d}}_{rb}\|^2\bar{\boldsymbol{d}}_{rb}^T\boldsymbol{d}_{rb}}{\bar{p}_{b,k}^2} - \frac{2(\|\bar{\boldsymbol{d}}_{rb}\|^2)^2 p_{b,k}}{\bar{p}_{b,k}^3} - \frac{(\|\bar{\boldsymbol{d}}_{rb}\|^2)^2}{\bar{p}_{b,k}^2}\right) \\ &+\left(\frac{4\|\bar{\boldsymbol{d}}_{kr}\|^2\bar{\boldsymbol{d}}_{kr}^T\boldsymbol{d}_{kr}}{(\bar{p}_{r,k}^{\mathrm{D}})^2} - \frac{2(\|\bar{\boldsymbol{d}}_{kr}\|^2)^2 p_{r,k}^{\mathrm{D}}}{(\bar{p}_{r,k}^{\mathrm{D}})^3} - \frac{(\|\bar{\boldsymbol{d}}_{kr}\|^2)^2}{(\bar{p}_{r,k}^{\mathrm{D}})^2}\right)\Bigg], \end{aligned} \quad (25)$$

$$\begin{aligned}\bar{R}_k^{\mathrm{U}}(\boldsymbol{x}_r, p_{r,k}^{\mathrm{U}}) \triangleq\ & \log\left(1 + \xi^{-1}\left(\frac{2\bar{\boldsymbol{d}}_{kr}^T}{P_{u,k}}\boldsymbol{d}_{kr} - \frac{\|\bar{\boldsymbol{d}}_{kr}\|^2}{P_{u,k}}\right)\right) + \log\left(1 + \xi^{-1}\left(\frac{2\bar{\boldsymbol{d}}_{rb}^T}{\bar{p}_{r,k}^{\mathrm{U}}}\boldsymbol{d}_{rb} - \frac{\|\bar{\boldsymbol{d}}_{rb}\|^2}{(\bar{p}_{r,k}^{\mathrm{U}})^2}p_{r,k}^{\mathrm{U}}\right)\right) \\ &-\log(\bar{I}_k^{\mathrm{U}}) + 1 - \frac{1}{\bar{I}_k^{\mathrm{U}}\xi}\left(\frac{\|\boldsymbol{d}_{kr}\|^2}{P_{u,k}} + \frac{\|\boldsymbol{d}_{rb}\|^2}{p_{r,k}^{\mathrm{U}}}\right) - \frac{1}{2\bar{I}_k^{\mathrm{U}}\xi^2}\left(\frac{\|\boldsymbol{d}_{kr}\|^2}{P_{u,k}} + \frac{\|\boldsymbol{d}_{rb}\|^2}{p_{r,k}^{\mathrm{U}}}\right)^2 \\ &+\frac{1}{2\bar{I}_k^{\mathrm{U}}\xi^2}\Bigg[\left(\frac{4\|\bar{\boldsymbol{d}}_{kr}\|^2\bar{\boldsymbol{d}}_{kr}^T\boldsymbol{d}_{kr}}{P_{u,k}^2} - \frac{3(\|\bar{\boldsymbol{d}}_{kr}\|^2)^2}{P_{u,k}^2}\right) + \left(\frac{4\|\bar{\boldsymbol{d}}_{rb}\|^2\bar{\boldsymbol{d}}_{rb}^T\boldsymbol{d}_{rb}}{(\bar{p}_{r,k}^{\mathrm{U}})^2} - \frac{2(\|\bar{\boldsymbol{d}}_{rb}\|^2)^2 p_{r,k}^{\mathrm{U}}}{(\bar{p}_{r,k}^{\mathrm{U}})^3} - \frac{(\|\bar{\boldsymbol{d}}_{rb}\|^2)^2}{(\bar{p}_{r,k}^{\mathrm{U}})^2}\right)\Bigg]. \end{aligned} \quad (26)$$

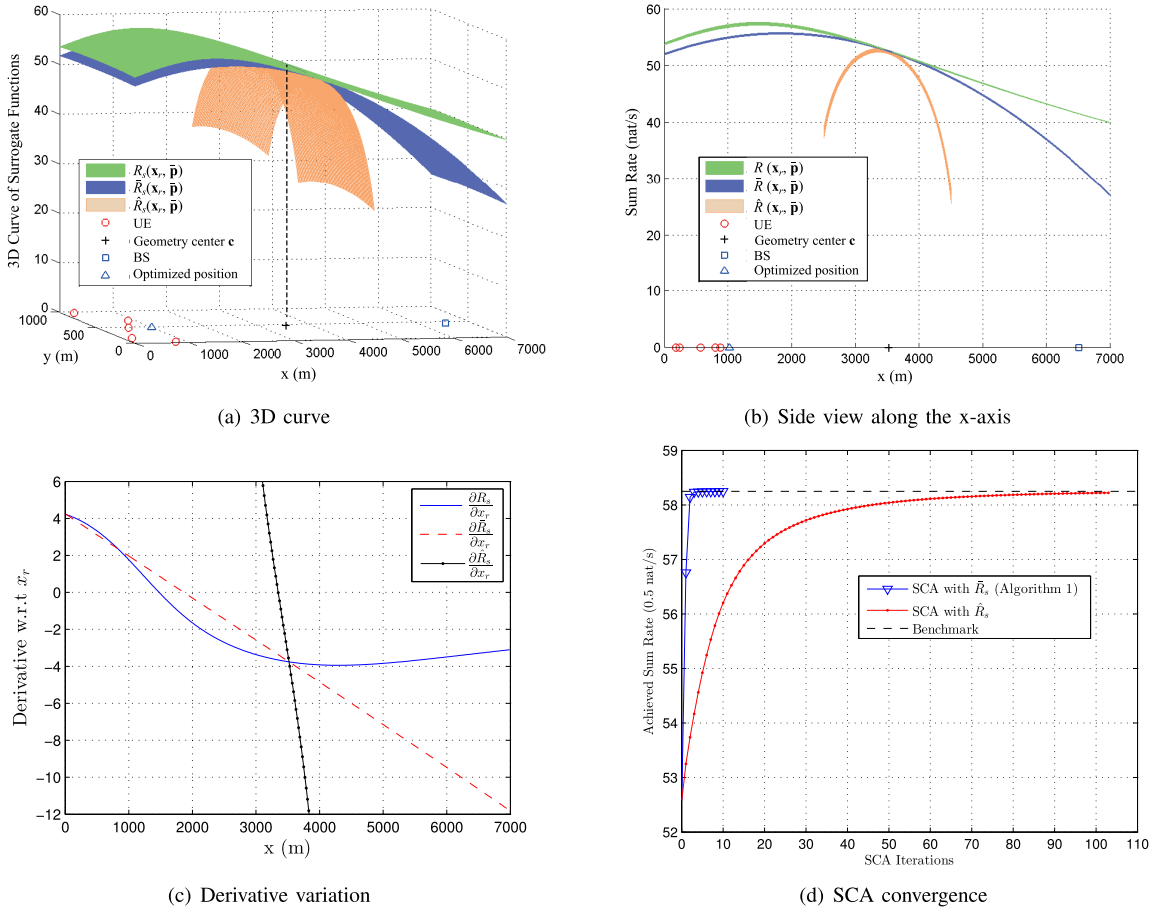

(a) 3D curve

(b) Side view along the x-axis

(c) Derivative variation

(d) SCA convergence

Fig. 2. (a)-(c) Illustration of the sum rate function $R_s(\boldsymbol{x}_r, \bar{\boldsymbol{p}})$ and the surrogate functions $\bar{R}_s(\boldsymbol{x}_r, \bar{\boldsymbol{p}})$ and $\hat{R}_s(\boldsymbol{x}_r, \bar{\boldsymbol{p}})$ with respect to the UAV position $\boldsymbol{x}_r$ for a scenario with $K = 5$ UEs; $\bar{R}_s(\boldsymbol{x}_r, \bar{\boldsymbol{p}})$ and $\hat{R}_s(\boldsymbol{x}_r, \bar{\boldsymbol{p}})$ are obtained by setting $\bar{\boldsymbol{x}}_r$ equal to the geometry center point and the power values are set to $\bar{p}^{\mathrm{D}}_{r,k} = \bar{p}^{\mathrm{U}}_{r,k} = P_r/(2K)$ and $p_{b,k} = P_b/K$ for all $k \in \mathcal{K}$. (d) Convergence curves of the proposed SCA algorithm using surrogate functions $\bar{R}_s(\boldsymbol{x}_r, \boldsymbol{p})$ in (23) and $\hat{R}_s(\boldsymbol{x}_r, \boldsymbol{p})$ in (30), respectively.

we focus on the UAV position variable $\boldsymbol{x}_r$ only and assume that the power variables $\boldsymbol{p}$ are fixed at the given value $\bar{\boldsymbol{p}}$. As mentioned, by [31, Theorem 3], the iteration complexity of the SCA algorithm to reach a stationary point is in the order of $\mathcal{O}(\frac{L^2}{\epsilon})$. If a surrogate function has a larger value of L, the surrogate function has a larger curvature and thus the SCA algorithm would progress slowly. The following result compares the curvature of the two surrogate functions at the given point $(\bar{\boldsymbol{x}}_r, \bar{\boldsymbol{p}})$.

Proposition 2: *Consider the surrogate functions* $\bar{R}_s(\boldsymbol{x}_r, \bar{\boldsymbol{p}})$ *in* (23) *and* $\hat{R}_s(\boldsymbol{x}_r, \bar{\boldsymbol{p}})$ *in* (30)*. When* ξ *is large, the spectral radius of the Hessian matrices* $\nabla^2_{\boldsymbol{x}_r}\bar{R}_s(\boldsymbol{x}_r, \bar{\boldsymbol{p}}))$ *and* $\nabla^2_{\boldsymbol{x}_r}\hat{R}_s(\boldsymbol{x}_r, \bar{\boldsymbol{p}}))$ *satisfy*

$$|\lambda_{\max}(\nabla^2_{\boldsymbol{x}_r}\bar{R}_s(\boldsymbol{x}_r, \bar{\boldsymbol{p}}))| \leq \mathcal{O}(\xi^{-1}) + c, \tag{34}$$

$$|\lambda_{\max}(\nabla^2_{\boldsymbol{x}_r}\hat{R}_s(\boldsymbol{x}_r, \bar{\boldsymbol{p}}))| \leq \mathcal{O}(1), \tag{35}$$

respectively, where $c > 0$ *is a constant. Moreover, when* $\boldsymbol{x}_r = \bar{\boldsymbol{x}}_r$ *and* $\xi \to \infty$*,*

$$|\lambda_{\max}(\nabla^2_{\boldsymbol{x}_r}\hat{R}_s(\bar{\boldsymbol{x}}_r, \bar{\boldsymbol{p}}))| > |\lambda_{\max}(\nabla^2_{\boldsymbol{x}_r}\bar{R}_s(\boldsymbol{x}_r, \bar{\boldsymbol{p}}))|. \tag{36}$$

Proof: The result is obtained by deriving upper and lower bounds of the Hessian matrices of the surrogate functions; details are given in Appendix D. ■

$$\begin{aligned}\hat{R}^{\mathrm{D}}_k(\boldsymbol{x}_r, a_{b,k}, a^{\mathrm{D}}_{r,k}) = {} & \log\left(1 + \xi\frac{2\bar{a}^{\mathrm{D}}_{r,k}}{\|\bar{\boldsymbol{d}}_{kr}\|^2}a^{\mathrm{D}}_{r,k} - \xi\frac{(\bar{a}^{\mathrm{D}}_{r,k})^2}{(\|\bar{\boldsymbol{d}}_{kr}\|^2)^2}\|\boldsymbol{d}_{kr}\|^2\right) + \log\left(1 + \xi\frac{2\bar{a}_{b,k}}{\|\bar{\boldsymbol{d}}_{rb}\|^2}a_{b,k} - \xi\frac{(\bar{a}_{b,k})^2}{(\|\bar{\boldsymbol{d}}_{rb}\|^2)^2}\|\boldsymbol{d}_{rb}\|^2\right) \\ & -\log\left(1+\bar{J}^{\mathrm{D}}_k\right) + \frac{\bar{J}^{\mathrm{D}}_k}{1+\bar{J}^{\mathrm{D}}_k} - \frac{\xi}{1+\bar{J}^{\mathrm{D}}_k}\left(\frac{(a^{\mathrm{D}}_{r,k})^2}{\|\boldsymbol{u}_k\|^2 - \|\bar{\boldsymbol{x}}_r\|^2 + 2(\bar{\boldsymbol{d}}_{kr})^T\boldsymbol{x}_r} + \frac{a^2_{b,k}}{\|\boldsymbol{b}\|^2 - \|\bar{\boldsymbol{x}}_r\|^2 + 2(\bar{\boldsymbol{d}}_{rb})^T\boldsymbol{x}_r}\right),\end{aligned} \tag{31}$$

$$\begin{aligned}\hat{R}^{\mathrm{U}}_k\left(\boldsymbol{x}_r, a^{\mathrm{U}}_{r,k}\right) = {} & \log\left(1 + \xi\frac{2\bar{a}^{\mathrm{U}}_{r,k}}{\|\bar{\boldsymbol{d}}_{rb}\|^2}a^{\mathrm{U}}_{r,k} - \xi\frac{(\bar{a}^{\mathrm{U}}_{r,k})^2}{(\|\bar{\boldsymbol{d}}_{rb}\|^2)^2}\|\boldsymbol{d}_{rb}\|^2\right) + \log\left(1 + \xi\frac{2P_{u,k}}{\|\bar{\boldsymbol{d}}_{kr}\|^2} - \xi\frac{P_{u,k}}{(\|\bar{\boldsymbol{d}}_{kr}\|^2)^2}\|\boldsymbol{d}_{kr}\|^2\right) \\ & -\log\left(1+\bar{J}^{\mathrm{U}}_k\right) + \frac{\bar{J}^{\mathrm{U}}_k}{1+\bar{J}^{\mathrm{U}}_k} - \frac{\xi}{1+\bar{J}^{\mathrm{U}}_k}\left(\frac{(a^{\mathrm{U}}_{r,k})^2}{\|\boldsymbol{b}\|^2 - \|\bar{\boldsymbol{x}}_r\|^2 + 2(\bar{\boldsymbol{d}}_{rb})^T\boldsymbol{x}_r} + \frac{P_{u,k}}{\|\boldsymbol{u}_k\|^2 - \|\bar{\boldsymbol{x}}_r\|^2 + 2(\bar{\boldsymbol{d}}_{kr})^T\boldsymbol{x}_r}\right).\end{aligned} \tag{32}$$

As ξ is typically a large number,[1] Proposition 2 shows that the curvature of the proposed surrogate function in (23) can be smaller than that of the surrogate function in (30) at the approximation point. While Proposition 2 gives only a limited claim, the curvature difference between the two surrogate functions can actually be large numerically. To demonstrate this, we draw in Fig. 2 (3D curve in Fig. 2(a) and side view along the x-axis in Fig. 2(b)) the sum rate function $R_s(\boldsymbol{x}_r, \bar{\boldsymbol{p}})$ and the surrogate functions $\bar{R}_s(\boldsymbol{x}_r, \bar{\boldsymbol{p}})$ and $\hat{R}_s(\boldsymbol{x}_r, \bar{\boldsymbol{p}})$ with respect to the UAV position $\boldsymbol{x}_r$ for a scenario with $K = 5$ UEs. The derivative of the three functions are further plotted in Fig. 2(c). The simulation setting is the same as that in Section V. First of all, one can see that the sum rate function $R_s(\boldsymbol{x}_r, \bar{\boldsymbol{p}})$ is non-concave, especially by observing that $\frac{\partial R_s}{\partial x_r}$ turns from decreasing to increasing around $x_r = 4300$ m in Fig. 2(c), whereas the two surrogate functions $\bar{R}_s(\boldsymbol{x}_r, \bar{\boldsymbol{p}})$ and $\hat{R}_s(\boldsymbol{x}_r, \bar{\boldsymbol{p}})$ are indeed concave and locally tight lower bounds of $R_s(\boldsymbol{x}_r, \bar{\boldsymbol{p}})$. Secondly, at the given point of $\bar{\boldsymbol{x}}_r$ which is equal to the geometry center $\mathbf{c} \triangleq (\frac{1}{K}\sum_{k=1}^{K} \boldsymbol{u}_k + \boldsymbol{b})/2$, the proposed surrogate function $\bar{R}_s(\boldsymbol{x}_r, \bar{\boldsymbol{p}})$ is much less curvy than the surrogate function $\hat{R}_s(\boldsymbol{x}_r, \bar{\boldsymbol{p}})$. Besides, comparing to $\hat{R}_s(\boldsymbol{x}_r, \bar{\boldsymbol{p}})$, the maximum function value of $\bar{R}_s(\boldsymbol{x}_r, \bar{\boldsymbol{p}})$ is closer to that of $R_s(\boldsymbol{x}_r, \bar{\boldsymbol{p}})$. Therefore, in accordance with [31, Theorem 3], one can anticipate that the SCA algorithm using $\bar{R}_s(\boldsymbol{x}_r, \boldsymbol{p})$ would exhibit a faster convergence behavior.

In Fig. 2(d), we further show the convergence curves (achieved sum rate versus iteration number) of the SCA algorithms using surrogate functions $\bar{R}_s(\boldsymbol{x}_r, \bar{\boldsymbol{p}})$ and $\hat{R}_s(\boldsymbol{x}_r, \bar{\boldsymbol{p}})$, respectively. Once can observe from the figure that the two converge curves are drastically different – the SCA algorithm using $\bar{R}_s(\boldsymbol{x}_r, \bar{\boldsymbol{p}})$, i.e., Algorithm 1, quickly converges with around 15 iterations whereas that using $\hat{R}_s(\boldsymbol{x}_r, \bar{\boldsymbol{p}})$ takes around 100 iterations to reach the same value of sum rate. These numerical results corroborate Proposition 2. Given the encouraging results in Proposition 2 and Fig. 2(d), it is interesting to think about in the future whether there is a general guideline for finding a good surrogate function for fast SCA.

C. Double-Loop Accelerated Gradient Projection

As discussed in Remark 1, for the convex approximation problem (27), one may solve its Lagrange dual problem via the DSA method. However, due to the iterative SCA updates in Algorithm 1, the DSA algorithm needs to be called for every iteration of SCA. Recently, the authors of [32] proposed an algorithm that combines the SCA approximation and the FISTA-type accelerated gradient projection (AGP) algorithm [33]. The algorithm, which is referred to as gradient extrapolated majorization-minimization (GEMM), can in practice converge faster than the algorithm that uses AGP to solve the convex approximation problem in every SCA iteration. In this subsection, we extend the idea of GEMM to our UAV JPPC problem (11), and propose a double-loop AGP method.

[1]For $\beta = -40$ dB and $\sigma^2 = -169$ dBm/Hz $\times$ 10 MHz $= -99$ dBm, ξ is approximately 10^9.

For ease of exposition, let us write (11) compactly as

$$\max_{\boldsymbol{y}} \; R_s(\boldsymbol{y}) \;\; \text{s.t. } \boldsymbol{y} \in \mathcal{Y}, \tag{37}$$

where $\boldsymbol{y} \triangleq (\boldsymbol{x}_r^T, \left(\boldsymbol{p}_r^{\mathrm{U}}\right)^T, \left(\boldsymbol{p}_r^{\mathrm{D}}\right)^T, \boldsymbol{p}_b^T)^T$, and

$$\mathcal{Y} \triangleq \left\{ \boldsymbol{y} \left| \begin{array}{l} \mathbf{1}^T\boldsymbol{p}_r^U + \mathbf{1}^T\boldsymbol{p}_r^{\mathrm{D}} + \frac{\gamma_c}{\xi'}\|\boldsymbol{x}_r - \boldsymbol{b}\|^2 \le P_r, \\ \mathbf{1}^T\boldsymbol{p}_b + \frac{\gamma_c}{\xi'}\|\boldsymbol{x}_r - \boldsymbol{b}\|^2 \le P_b, \; \boldsymbol{p} \ge 0 \end{array} \right. \right\}. \tag{38}$$

Moreover, we write the surrogate function $\bar{R}_s(\boldsymbol{x}_r, \boldsymbol{p})$ in (27a) as $\bar{R}_s(\boldsymbol{y}; \bar{\boldsymbol{y}})$. By [32], the GEMM involves the following iterative updates: for $i = 1, 2, \ldots,$

$$\boldsymbol{z}^i = \boldsymbol{y}^i + \frac{i-1}{i+2}\left(\boldsymbol{y}^i - \boldsymbol{y}^{i-1}\right), \tag{39}$$

$$\boldsymbol{y}^{i+1} = \Pi_{\mathcal{Y}}\left[\boldsymbol{z}^i + \frac{1}{\tau_i}\nabla_{\boldsymbol{y}}\bar{R}_s\left(\boldsymbol{z}^i; \boldsymbol{y}^i\right)\right], \tag{40}$$

where $\tau_i > 0$ is a step size which satisfies

$$\bar{R}_s\left(\boldsymbol{y}^{i+1}; \boldsymbol{y}^i\right) \ge \bar{R}_s\left(\boldsymbol{z}^i; \boldsymbol{y}^i\right) + \nabla_{\boldsymbol{y}}\bar{R}_s^T\left(\boldsymbol{z}^i; \boldsymbol{y}^i\right)\left(\boldsymbol{y}^{i+1} - \boldsymbol{z}^i\right) - \frac{\tau_i}{2}\|\boldsymbol{y}^{i+1} - \boldsymbol{z}^i\|^2, \tag{41}$$

$\Pi_{\mathcal{Y}}$ is the projection operation onto the set of $\mathcal{Y}$, and it is defined that

$$\boldsymbol{z}^i \triangleq ((\boldsymbol{z}_x^i)^T, (\boldsymbol{z}_p^i)^T)^T = ((\boldsymbol{z}_x^i)^T, (\boldsymbol{z}_p^{\mathrm{U},i})^T, (\boldsymbol{z}_p^{\mathrm{D},i})^T, (\boldsymbol{z}_p^{\mathrm{b},i})^T)^T,$$

$$\nabla_{\boldsymbol{y}}\bar{R}_s\left(\boldsymbol{z}^i; \boldsymbol{y}^i\right) \triangleq \begin{bmatrix} \nabla_{\boldsymbol{x}_r}\bar{R}_s\left(\boldsymbol{z}^i; \boldsymbol{y}^i\right) \\ \nabla_{\boldsymbol{p}_r^{\mathrm{U}}}\bar{R}_s\left(\boldsymbol{z}^i; \boldsymbol{y}^i\right) \\ \nabla_{\boldsymbol{p}_r^{\mathrm{D}}}\bar{R}_s\left(\boldsymbol{z}^i; \boldsymbol{y}^i\right) \\ \nabla_{\boldsymbol{p}_b}\bar{R}_s\left(\boldsymbol{z}^i; \boldsymbol{y}^i\right) \end{bmatrix}.$$

As seen, the GEMM algorithm would be computationally efficient if (40) admits a closed-form solution, e.g., when the constraint set $\mathcal{Y}$ is simple such as box constraints.

While the set $\mathcal{Y}$ in (38) is not simple, (40) may still be handled efficiently since it is a convex quadratically constrained quadratic program (QCQP). In particular, let us write (40) explicitly as

$$\boldsymbol{y}^{i+1} = \arg\min_{\boldsymbol{x}_r, \boldsymbol{p} \ge 0} \left\{ \begin{array}{l} \|\boldsymbol{x}_r - (\boldsymbol{z}_x^i + \frac{1}{\tau_i}\nabla_{\boldsymbol{x}_r}\bar{R}_s\left(\boldsymbol{z}^i; \boldsymbol{y}^i\right))\|^2 \\ +\|\boldsymbol{p} - (\boldsymbol{z}_p^i + \frac{1}{\tau_i}\nabla_{\boldsymbol{p}}\bar{R}_s\left(\boldsymbol{z}^i; \boldsymbol{y}^i\right))\|^2 \end{array} \right\}$$

$$\text{s.t. } \mathbf{1}^T\boldsymbol{p}_r^{\mathrm{U}} + \mathbf{1}^T\boldsymbol{p}_r^{\mathrm{D}} + \frac{\gamma_c}{\xi'}\|\boldsymbol{x}_r - \boldsymbol{b}\|^2 \le P_r, \tag{42a}$$

$$\mathbf{1}^T\boldsymbol{p}_b + \frac{\gamma_c}{\xi'}\|\boldsymbol{x}_r - \boldsymbol{b}\|^2 \le P_b. \tag{42b}$$

Let $\lambda \ge 0$ and $\mu \ge 0$ be the dual variables associated with (42a) and (42b), respectively, and let $\nu_{rk}^{\mathrm{D}}, \nu_{rk}^{\mathrm{U}}, \nu_{bk} \ge 0$ to be the dual variables associated with constraints $p_{rk}^{\mathrm{D}}, p_{rk}^{\mathrm{U}}, p_{bk} \ge 0$ for all $k \in \mathcal{K}$. The Lagrangian of (42) is

$$\begin{aligned} \mathcal{L}^i\left(\boldsymbol{y}, \lambda, \mu, \boldsymbol{\nu}\right) = {} & \|\boldsymbol{x}_r - (\boldsymbol{z}_x^i + \frac{1}{\tau_i}\nabla_{\boldsymbol{x}_r}\bar{R}_s\left(\boldsymbol{z}^i; \boldsymbol{y}^i\right))\|^2 \\ & + \|\boldsymbol{p} - (\boldsymbol{z}_p^i + \frac{1}{\tau_i}\nabla_{\boldsymbol{p}}\bar{R}_s\left(\boldsymbol{z}^i; \boldsymbol{y}^i\right))\|^2 \\ & + \lambda\left(\mathbf{1}^T\boldsymbol{p}_r^{\mathrm{U}} + \mathbf{1}^T\boldsymbol{p}_r^{\mathrm{D}} + \frac{\gamma_c}{\xi'}\|\boldsymbol{x}_r - \boldsymbol{b}\|^2 - P_r\right) \\ & + \mu\left(\mathbf{1}^T\boldsymbol{p}_b + \frac{\gamma_c}{\xi'}\|\boldsymbol{x}_r - \boldsymbol{b}\|^2 - P_b\right) \\ & - (\boldsymbol{\nu}_r^{\mathrm{D}})^T\boldsymbol{p}_r^{\mathrm{D}} - (\boldsymbol{\nu}_r^{\mathrm{U}})^T\boldsymbol{p}_r^{\mathrm{U}} - (\boldsymbol{\nu}_b)^T\boldsymbol{p}_b. \end{aligned} \tag{43}$$

Then, the dual problem of (42) is given by

$$\max_{(\lambda,\mu,\boldsymbol{\nu})\geq 0} \left\{\min_{\boldsymbol{y}} \mathcal{L}^i(\boldsymbol{y},\lambda,\mu,\boldsymbol{\nu})\right\} \triangleq \max_{(\lambda,\mu,\boldsymbol{\nu})\geq 0} g^i(\lambda,\mu,\boldsymbol{\nu}), \quad (44)$$

where $g(\lambda,\mu,\boldsymbol{\nu})$ is the dual function and can be obtained as

$$\begin{aligned} g^i(\lambda,\mu,\boldsymbol{\nu}) = & \frac{(\lambda+\mu)\frac{\gamma_c}{\xi'}}{1+(\lambda+\mu)\frac{\gamma_c}{\xi'}}\|\boldsymbol{b}-(\boldsymbol{z}_x^i+\frac{1}{\tau_i}\nabla_{\boldsymbol{x}_r}\bar{R}_s\left(\boldsymbol{z}^i;\boldsymbol{y}^i\right))\|^2 \\ & -\frac{1}{4}\|\lambda\mathbf{1}-\boldsymbol{\nu}_r^{\mathrm{U}}\|^2-\frac{1}{4}\|\lambda\mathbf{1}-\boldsymbol{\nu}_r^{\mathrm{D}}\|^2 \\ & +(\boldsymbol{z}_p^{\mathrm{U},i}+\frac{1}{\tau_i}\nabla_{\boldsymbol{p}_r^{\mathrm{U}}}\bar{R}_s\left(\boldsymbol{z}^i;\boldsymbol{y}^i\right))^T(\lambda\mathbf{1}-\boldsymbol{\nu}_r^{\mathrm{U}}) \\ & +(\boldsymbol{z}_p^{\mathrm{D},i}+\frac{1}{\tau_i}\nabla_{\boldsymbol{p}_r^{\mathrm{D}}}\bar{R}_s\left(\boldsymbol{z}^i;\boldsymbol{y}^i\right))^T(\lambda\mathbf{1}-\boldsymbol{\nu}_r^{\mathrm{D}}) \\ & -\frac{1}{4}\|\mu\mathbf{1}-\boldsymbol{\nu}_b\|^2-\lambda P_r-\mu P_b \\ & +(\boldsymbol{z}_p^{b,i}+\frac{1}{\tau_i}\nabla_{\boldsymbol{p}_b}\bar{R}_s\left(\boldsymbol{z}^i;\boldsymbol{y}^i\right))^T(\mu\mathbf{1}-\boldsymbol{\nu}_b). \quad (45) \end{aligned}$$

It is interesting to see that the dual function has a closed-form expression, thanks to the quadratic objective function and constraints in (42). Instead of (42), we solve the dual problem (44). Specifically, since (44) is a smooth convex optimization problem, we propose to solve (44) using the AGP method [33]. Once (44) is solved, the corresponding primal solutions to (42) are the unique minimizer of $\min_{\boldsymbol{y}} \mathcal{L}^i(\boldsymbol{y},\lambda,\mu,\boldsymbol{\nu})$, which are given by

$$\boldsymbol{x}_r = \frac{\boldsymbol{z}_x^i+\frac{1}{\tau_i}\nabla_{\boldsymbol{x}_r}\bar{R}_s\left(\boldsymbol{z}^i;\boldsymbol{y}^i\right)+(\lambda+\mu)\frac{\gamma_c}{\xi'}\boldsymbol{b}}{1+(\lambda+\mu)\frac{\gamma_c}{\xi'}}, \quad (46a)$$

$$\boldsymbol{p}_r^{\mathrm{U}} = \boldsymbol{z}_p^{\mathrm{U},i}+\frac{1}{\tau_i}\nabla_{\boldsymbol{p}_r^{\mathrm{U}}}\bar{R}_s\left(\boldsymbol{z}^i;\boldsymbol{y}^i\right)-\frac{1}{2}(\lambda\mathbf{1}-\boldsymbol{\nu}_r^{\mathrm{U}}), \quad (46b)$$

$$\boldsymbol{p}_r^{\mathrm{D}} = \boldsymbol{z}_p^{\mathrm{D},i}+\frac{1}{\tau_i}\nabla_{\boldsymbol{p}_r^{\mathrm{D}}}\bar{R}_s\left(\boldsymbol{z}^i;\boldsymbol{y}^i\right)-\frac{1}{2}(\lambda\mathbf{1}-\boldsymbol{\nu}_r^{\mathrm{D}}), \quad (46c)$$

$$\boldsymbol{p}_b = \boldsymbol{z}_p^{b,i}+\frac{1}{\tau_i}\nabla_{\boldsymbol{p}_b}\bar{R}_s\left(\boldsymbol{z}^i;\boldsymbol{y}^i\right)-\frac{1}{2}(\mu\mathbf{1}-\boldsymbol{\nu}_b). \quad (46d)$$

In summary, by combining the GEMM algorithm in (39) and (40), and using the dual AGP algorithm to handle (40), we obtain Algorithm 2 for solving our UAV JPPC problem (11) which involves double loops of AGP steps. In Algorithm 2, we denote $\mathbf{s}=(\lambda,\mu,\boldsymbol{\nu}^T)^T, g^i(\lambda,\mu,\boldsymbol{\nu})=g^i(\mathbf{s};\boldsymbol{z}^i,\boldsymbol{y}^i,\tau_i)$, and $\mathcal{S}=\{\mathbf{s}|\lambda\geq 0,\mu\geq 0,\boldsymbol{\nu}\geq 0\}$, for notation simplicity.

Before ending this section, we have the following remark regarding one future direction.

Remark 2: Like the majority of the literature, the current work has assumed the LoS channels and fixed the flying altitude of the relay UAV. It is known that, under a more realistic probabilistic LoS channel model [26], [27], the flying altitude directly affects the probability of LoS and non-LoS links. Here let us show the challenges for solving the JPPC problem if the probabilistic LoS channel model is considered. Denote β_χ as the reference channel gain, where $\chi\in\{\mathrm{LoS},\mathrm{NLoS}\}$ is the path loss type. Using the uplink link (1)-(4) as the example, suppose that the UE-UAV channel is of path loss χ and the UAV-BS channel is of path loss χ', the corresponding uplink rate is

$$R_{\chi\chi',k}\triangleq\log\left(1+\frac{\beta_\chi\beta_{\chi'}p_{r,k}^{\mathrm{U}}p_{u,k}d_{kr}^{-2}d_{rb}^{-2}}{\beta_{\chi'}p_{r,k}^{\mathrm{U}}d_{rb}^{-2}\sigma^2+\beta_\chi p_{u,k}d_{kr}^{-2}\sigma^2+(\sigma^2)^2}\right).$$

Algorithm 2 Proposed Double-Loop AGP for Problem (11)

1: **Initilize** $i=1,\kappa,\tau_1$ and $\boldsymbol{y}^1=\boldsymbol{y}^0$ that is feasible to (11);
2: **repeat**
3: $\boldsymbol{z}^i=\boldsymbol{y}^i+\frac{i-1}{i+2}(\boldsymbol{y}^i-\boldsymbol{y}^{i-1})$;
4: Initialize $\ell=1,\mathbf{s}^1=\mathbf{s}^0=\mathbf{0}$;
5: **repeat**
6: $\boldsymbol{t}^\ell=\mathbf{s}^\ell+\frac{\ell-1}{\ell+2}(\mathbf{s}^\ell-\mathbf{s}^{\ell-1})$;
7: $\mathbf{s}^{\ell+1}=\Pi_{\mathcal{S}}\left[\boldsymbol{t}^\ell+\frac{1}{\eta_l}\nabla_{\mathbf{s}}g^i(\boldsymbol{t}^\ell;\boldsymbol{z}^i,\boldsymbol{y}^i,\tau_i)\right]$, where η_l is obtained by backtracking line search;
8: $\ell\leftarrow\ell+1$;
9: **until** $\frac{|g^i(\mathbf{s}^\ell;\boldsymbol{z}^i,\boldsymbol{y}^i,\tau_i)-g^i(\mathbf{s}^{\ell-1};\boldsymbol{z}^i,\boldsymbol{y}^i,\tau_i)|}{|g^i(\mathbf{s}^{\ell-1};\boldsymbol{z}^i,\boldsymbol{y}^i,\tau_i)|}\leq\epsilon_1$.
10: Obtain $\boldsymbol{y}^{i+1}$ by (46) using $\mathbf{s}^{\ell+1}=(\lambda^{\ell+1},\mu^{\ell+1},(\nu^{\ell+1})^T)^T$ and $(\boldsymbol{z}^i,\boldsymbol{y}^i)$;
11: **if** (41) is not met **then**
12: $\tau_i\leftarrow\kappa\tau_i$, $\boldsymbol{y}^i\leftarrow\boldsymbol{y}^{i+1}$, go to step 4;
13: **end if**
14: $\tau_{i+1}\leftarrow\tau_i$, $i\leftarrow i+1$;
15: **until** $|R_s(\boldsymbol{y}^i)-R_s(\boldsymbol{y}^{i-1})|\leq\epsilon_2$.

Since this holds with probability $P_{\chi\chi',k}=P_\chi(\boldsymbol{x}_r,\boldsymbol{u}_k)P_{\chi'}(\boldsymbol{x}_r,\boldsymbol{b})$, the average uplink rate for UE k is given by

$$\sum_{\chi,\chi'\in\{\mathrm{LOS},\mathrm{NLOS}\}} P_{\chi\chi',k}R_{\chi\chi',k}. \quad (47)$$

Here, $P_{\mathrm{NLoS}}(\boldsymbol{x}_r,\boldsymbol{u}_k)=1-P_{\mathrm{LoS}}(\boldsymbol{x}_r,\boldsymbol{u}_k)$, and according to [26].

$$P_{\mathrm{LoS}}(\boldsymbol{x}_r,\boldsymbol{u}_k) = \frac{1}{1+a\exp\left(-b\left(\tan^{-1}\left(\frac{h}{\sqrt{(x_r-x_k)^2+(y_r-y_k)^2}}\right)-a\right)\right)}, \quad (48)$$

where $a,b>0$ are some constants, is the probability to have LoS link between the UAV and UE k. The average rate in (47) includes the four combinations of the channel between the UAV and UE k and that between the UAV and the BS. While the proposed surrogate function in Section IV-A can be applied to approximate the log-term in (47), the overall average rate would not be concave due to the additional probability functions. There needs new approximation techniques to handle the associated JPPC problem.

V. Simulation Results

In the section, simulation results are presented to evaluate the performance of the proposed algorithms. In the simulation the reference channel power gain at the distance $1\ m$ from the transmitter is set to be $\beta=\beta'=-40$ dB. The frequency bandwidth allocated to each UE is $W=1$ MHz. The power spectrum density (PSD) of the noise power is -169 dBm/Hz. For convenience, tuples with the format $[x_{\min},x_{\max},y_{\min},y_{\max}]$ are used to define the range of locations of the UEs and the BS. UEs are randomly located in the rectangular area $[0,1000,0,1000]\ m$, and the BS is randomly located in the rectangular area $[6000,7000,0,1000]\ m$. The UEs and the BS are assumed to be on the ground. The UAV hovers at

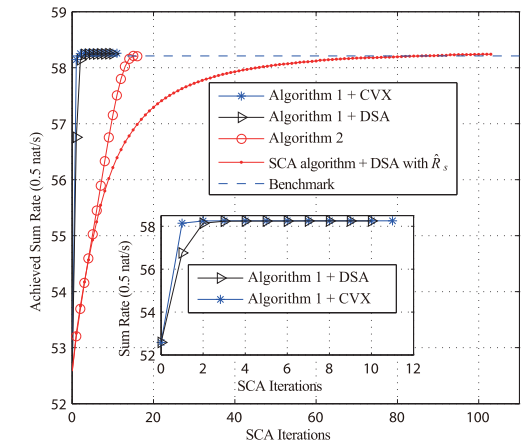

(a)

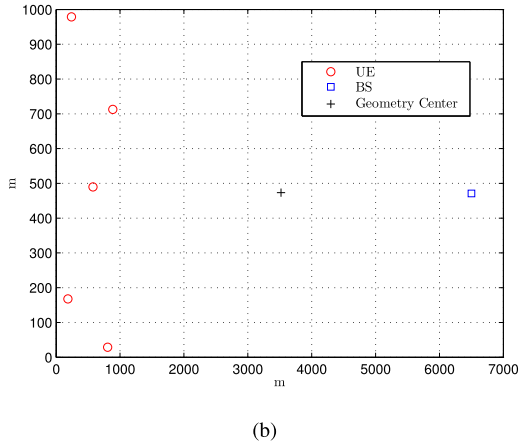

(b)

Fig. 3. (a) Sum rate versus iterations of SCA; $K = 5$, $\gamma_c = 20$ dB. (b) Top view of the topology with $K = 5$ UEs.

a fixed altitude that is set as $h = 100\ m$. Unless otherwise specified, the power budgets of each UE, the UAV and the BS are set to $P_{u,k} = 23$ dBm, $P_r = 36$ dBm and $P_b = 43$ dBm, respectively.

A. Convergence and Computation Time

Similar to Fig. 2(d), we first examine the converge of the proposed SCA algorithm (Algorithm 1) and double-loop AGP algorithm (Algorithm 2). For Algorithm 1, we consider the use of CVX solver [40] to solve problem (27) (denoted by Algorithm 1 + CVX), as well as the use of the DSA method described in Remark 1 (denoted by Algorithm 1 + DSA). The initial position of UAV $\boldsymbol{x}_r$ is set to the geometry center $\mathbf{c} \triangleq (\frac{1}{K}\sum_{k=1}^{K} \boldsymbol{u}_k + \boldsymbol{b})/2$, and the initial transmit powers of the UAV and that of the BS are uniformly allocated for each UE. The stopping criterion ϵ_0 in Algorithm 1 is set to 10^{-3}. The initial conditions for Algorithm 2 are the same as those for Algorithm 1, with additional parameter κ set to 1.2, and τ_1 is chosen such that the inequality (41) holds for $\boldsymbol{y}^1$ and $\boldsymbol{y}^0$. The stopping criterion in Algorithm 2 is set to $\epsilon_1 = 5 \times 10^{-3}$ and $\epsilon_2 = 10^{-3}$.

Fig. 3(a) shows the achieved sum rates versus the SCA iteration of Algorithm 1 + CVX, Algorithm 1 + DSA, and Algorithm 2. The SCA algorithm using $\hat{R}_s$ as the surrogate function and using DSA for solving (27) is also presented, denoted by 'SCA algorithm + DSA with $\hat{R}_s$'. The curve of benchmark is the converged sum rate achieved by Algorithm 1 + CVX. The locations of UEs and BS are shown in Fig. 3(b) for $K = 5$ and $\gamma_c = 20$ dB. One can see that the sum rates increase with the iteration numbers. The curve of Algorithm 1 + DSA is similar to that of Algorithm 1 + CVX. They respectively take 10 iterations and 11 iterations to reach the benchmark. Interestingly, Algorithm 2 can even converge faster than the SCA algorithm + DSA with $\hat{R}_s$. Fig. 4 displays similar results for a scenario with 16 UEs $K = 16$.

TABLE I
COMPARISON ON THE AVERAGE COMPUTATION TIME

Number of UEs (K)	5	10	16
SCA algorithm + DSA with $\hat{R}_s$	36.06 s	58.78 s	114.18 s
Algorithm 1 + DSA	4.28 s	7.21 s	11.38 s
Algorithm 2	0.10 s	0.17 s	0.25 s

In Table I, the average running time of SCA algorithm + DSA with $\hat{R}_s$, Algorithm 1 + DSA, and Algorithm 2 are presented for different numbers of UEs. The results are obtained by averaging 70 random simulation trials, conducted on a laptop computer with a 2-core 2.50 GHz CPU and 4 GB RAM. As seen, consistent with the results in Fig. 3(a) and Fig. 4(a), Algorithm 1 + DSA is much more computationally efficient than the SCA algorithm + DSA with $\hat{R}_s$. Moreover, Algorithm 2 is about 40 times faster than Algorithm 1 + DSA in terms of the running time.

B. Performance of Wireless Two-Way Relaying

Example 1: In Fig. 5, we display the achieved sum rate as well as the optimized UAV positions versus the BS transmit power budget P_b, for a scenario with 16 UEs ($K = 16$) and control link constraint $\gamma_c = 10$ and 20 dB [35], [36], respectively. Except for the proposed Algorithm 2 which jointly optimizes the UAV position and transmission powers of all terminals, we also present the results that the UAV is fixed either on the top of the BS (Above BS) or at the geometry center (GeoCenter). When the UAV's position is fixed above BS, we either consider fixed uniform power allocation (UniPw) or optimized power allocation (OptPw) for the BS and UAV. In addition, the method in [28], which optimizes the power variables and the UAV position by SCA in an alternating fashion, is also implemented by CVX for comparison. The method is referred to as 'AltOpt'. Moreover, another 'ExSearch + OptPw' method is implemented as a performance benchmark. The method is conducted in an exhaustive search manner. Specifically, the UAV position is enumerated at a 2D grid with 10 m spacing over the topology and the power is optimized given each UAV candidate position.

One can observe in Fig. 5(a) that the sum rates achieved by most of the methods significantly increase with a larger P_b, whereas increments of the sum rates by 'Above BS, OptPw' and 'Above BS, UniPw' are negligible since the UAV-to-UE link causes the performance bottleneck due to the large difference between d_{kr} and d_{rb} when the UAV hovers above

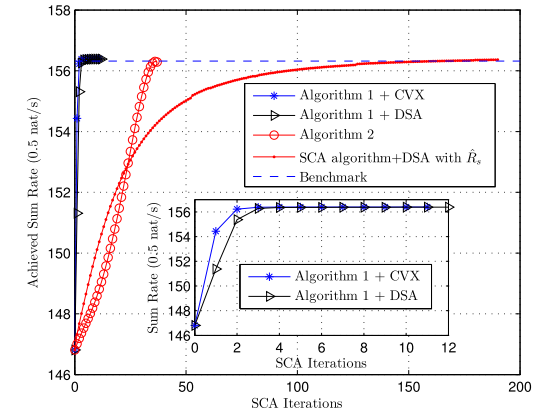

(a)

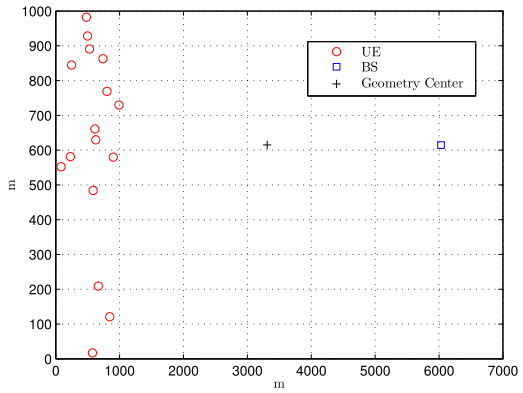

(b)

Fig. 4. (a) Sum rate versus number of SCA iterations; $K = 16$, $\gamma_c = 20$ dB. (b) Top view of the topology with $K = 16$ UEs.

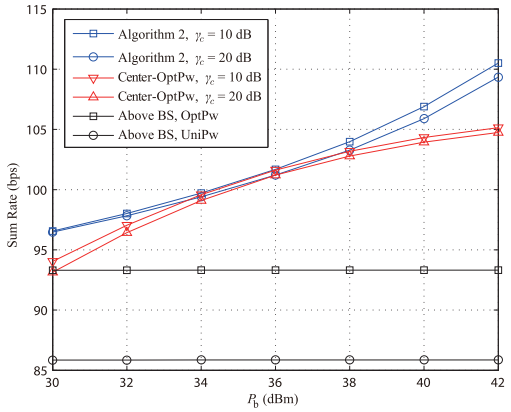

(a)

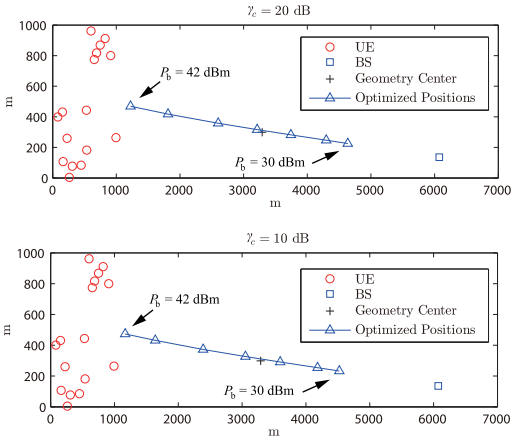

(b)

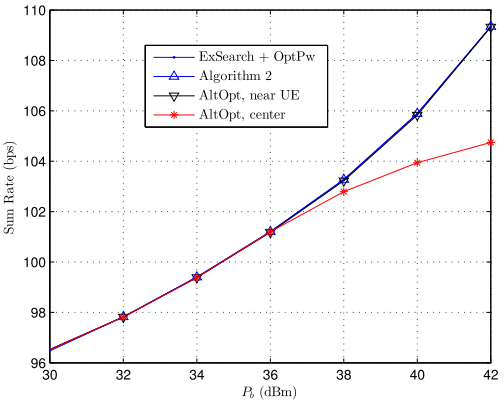

(c)

Fig. 5. (a) Sum rate versus the power budget of BS P_b. (b) Top view of the topology with $K = 16$ UEs and the optimized UAV position under different BS power budget P_b. (c) Sum rate versus the power budget of BS P_b, $\gamma_c = 20$ dB.

the BS. It can also be seen that the proposed Algorithm 2 can always achieve the best performance, comparing to all the other methods since in Algorithm 2 the transmission power and the UAV position are jointly optimized. In Fig. 5(b), it is observed that the optimized position of UAV tends to move closer to UEs if a larger P_b is given. As the optimized UAV positions are around the geometry center when P_b ranges from 34 dBm to 38 dBm, the sum rate achieved by Algorithm 2 is only slightly higher than that achieved by the method 'Center-OptPw' as seen from Fig. 5(a). In addition, in Fig. 5(c), Algorithm 2 always achieves almost the same sum rate as the 'ExSearch + OptPw' method. However, it is observed that the performance of the 'AltOpt' method varies under different initial UAV positions, among which 'center' denotes the Geo-Center and 'near UE' denotes an initial UAV postion $\mathbf{n}$ near the UEs, i.e., $\mathbf{n} \triangleq (\sum_{k=1}^{K} \boldsymbol{u}_k + \boldsymbol{b})/(K+1)$. One can see that 'AltOpt, near UE' can achieve almost the same performance as Algorithm 2 and 'ExSearch + OptPw', whereas the sum rate of 'AltOpt, center' decreases when $P_b > 36$ dBm. The performance loss is mainly due to the alternating optimization adopted by 'AltOpt'. This phenomenon can be further verified by Fig. 6(a) and Fig. 6(b). In Fig. 6(a), the convergence behavior of Algorithm 1 + CVX is given for comparison. One can see Algorithm 1 + CVX always has similar convergence behaviors, while 'AltOpt, center' will converge to a local point with a smaller sum rate. From Fig. 6(b), one can see that the optimized UAV position is stuck around the initial GeoCenter. It is noted that even 'AltOpt, near UE' obtains a sum rate nearly equal to that by Algorithm 1 + CVX (also Algorithm 2), the former one takes more iterations and time. Indeed, the time taken by 'AltOpt, near UE' is about 4 times larger than Algorithm 1 + CVX in the simulation. In Fig. 6(b),

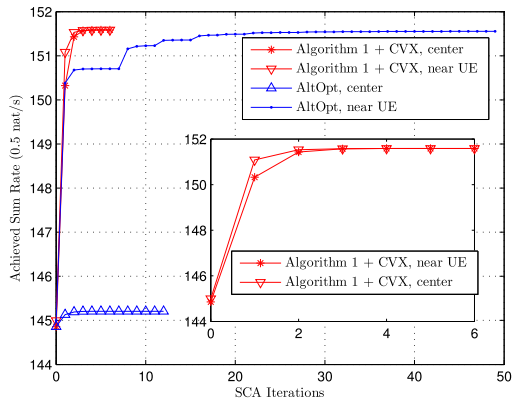

(a)

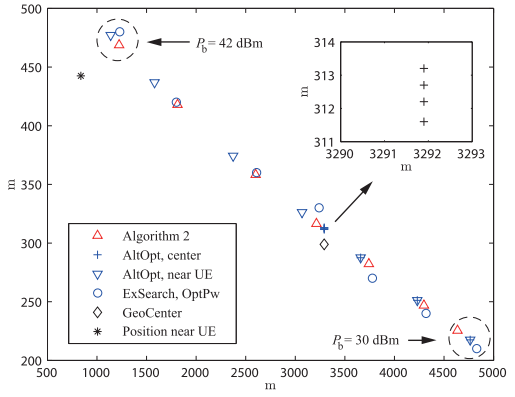

(b)

Fig. 6. (a) Convergence behavior of 'AltOpt' given different initial point, P_b = 42 dBm and $\gamma_c = 20$ dB. (b) The optimized position of UAV achieved by different methods, under the BS power budge P_b and $\gamma_c = 20$ dB.

it is found that the optimized UAV locations by these methods except 'AltOpt, center' are close to each other under the same P_b.

To examine the impact of the control link, the optimal positions achieved by Algorithm 1 under different values of γ_c are also given in Fig. 5(b). One can see that with a less stringent control link SNR requirement ($\gamma_c = 10$ dB), the UAV can move further from the BS and closer to UEs, bringing a higher sum rate as shown in Fig. 5(a). Thus, the control link plays an important role in the resource allocation of the UAV-enabled relaying communications and should not be overlooked.

Example 2: In Fig. 7(a), the sum rates versus the UAV budget P_r achieved by various schemes under consideration are displayed. The topology of UEs and BS is identical to that in Fig. 5(b). One can see that the sum rates obtained by all the algorithms increase with increasing P_r since more power can be allocated for information relaying. Besides, the proposed Algorithm 2 is superior than the other two schemes with fixed UAV position. It is noted that the sum rate by 'AltOpt, near UE' and 'ExSearch, OptPw' is almost the same with Algorithm 2 and not shown here to avoid putting many similar curves together and incurring confusion. One can also observe from Fig. 7(a) that the sum rate achieved by Algorithm 2 under

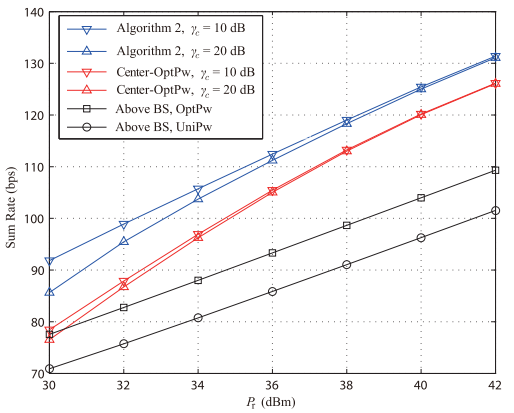

(a)

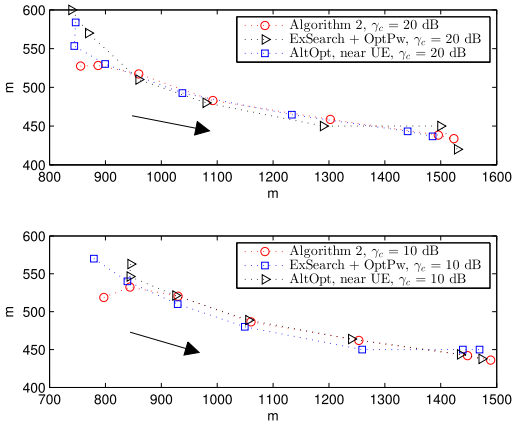

(b)

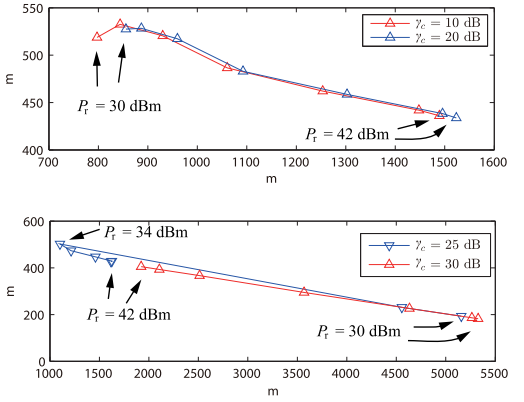

(c)

Fig. 7. (a) Sum rate versus the power budget of UAV P_r. (b) Top view of UAV positions obtained by different methods under different UAV power budget P_r and control link SNR requirement γ_c, (c) Top view of UAV positions obtained by Algorithm 2.

$\gamma = 10$ dB is higher than that under $\gamma = 20$ dB, especially when P_r is smaller. This is because the percentage of power that needs to be allocated for the control link is much larger when P_r is smaller and $\gamma = 20$ dB.

The optimized UAV positions by different methods are presented in Fig. 7(b), where the arrow points to the moving direction of optimized positions when P_r increases from

30 to 42 dBm. The UAV positions by the three methods at a given P_r are near with each other, in accordance with the similar performance of sum rate as mentioned above. It is also found that given a smaller P_r like 30 dBm, the distance between UAV positions by different methods gets larger while their obtained sum rate is still similar. One possible reason is that the sum rate is determined by both the UAV location and power control, and different combinations of the two may yeild similar performance of sum rate. Fig. 7(c) further shows the UAV positions optimized by Algorithm 2 in details and explores the impact from the control link. One can observe that when $\gamma_c = 10$ dB or $\gamma_c = 20$ dB, the optimized position of UAV will move closer to UE when P_r increases from 30 dBm to 42 dBm. However, as seen from Fig. 7(c), under $\gamma_c = 30$ dB, the moving direction of the optimized UAV position is opposite – it moves toward to the UEs when P_r increases. However, given $\gamma_c = 25$ dB, the optimized UAV position first moves closer to the UE, and then turns back to the BS at $P_r = 34$ dBm. In other words, the optimized UAV position is not trivially monotonic with respect to P_r. The reason is that the transmit power at the UAV is not only related to the control link signaling, but also affects the uplink and downlink data transmission.

VI. Conclusion

In the paper, we have investigated the JPPC problem (10) to maximize the sum rate of the UAV-enabled wireless two-way relay network. While the formulated problem (10) has a complicated sum rate function and is not concave, we have proposed the concave surrogate function in Proposition 1, and shown theoretically and numerically that the concave surrogate function can provide a significantly faster SCA convergence. To further improve the computational efficiency, we have exploited the quadratic constraint structure of (11) and developed a double-loop AGP algorithm (Algorithm 2). The double-loop AGP algorithm has a computation time that is at least an order of magnitude less than its counterpart based on SCA and DSA method. Moreover, the presented simulation results have shown how the BS power budget, UAV power budge and SNR requirement on the control link can affect the optimal relay UAV positioning. In particular, it is shown that the optimal UAV positioning is non-trivial since the optimized network sum rate can be greatly higher than those obtained by simple positioning strategies.

It is worthwhile to point out some interesting extensions. For instance, it would be interesting to incorporate bandwidth allocation for the UEs rather than the current fixed bandwidth allocation model in Section II-A. While joint bandwidth allocation would provide higher sum rate, it would lead to a more challenging optimization problem and new approximation techniques are needed. In addition, in view of that the full-duplex (FD) relaying can boost the spectrum efficiency as long as the self-interference can be effectively controlled, one may extend the JPPC problem to a FD UAV relay as in [43]. Lastly, it is also a promising direction to extend the JPPC problem to a scenario with multiple UAVs or with multiple coexisting BS-UAV pairs. The cross-link interference then have to be take into account and carefully handled.

Appendix A
Proof of Property 2

Denote $\boldsymbol{s} = \frac{\boldsymbol{b}-\boldsymbol{u}}{\|\boldsymbol{b}-\boldsymbol{u}\|} \triangleq (s_x, s_y, 0)^T$, and let $\boldsymbol{s}_\perp \triangleq (s'_x, s'_y, 0)^T$ be orthogonal to $\boldsymbol{s}$ and satisfy $\|\boldsymbol{s}_\perp\| = 1$. Then, the position of the UAV can be expressed as $\boldsymbol{x}_r = \boldsymbol{u} + \alpha\boldsymbol{s} + \alpha_\perp \boldsymbol{s}_\perp + h\boldsymbol{e}_z$, where $\boldsymbol{e}_z = (0,0,1)^T$ and $\alpha, \alpha_\perp \in \mathbb{R}$. For the denominator of the first logarithmic term in (14), we can bound it as follows

$$\begin{aligned}
&p_r^{\mathrm{U}} d_{ur}^2 + P_u d_{rb}^2 + \xi^{-1} d_{ur}^2 d_{rb}^2 \\
&= p_r^{\mathrm{U}} \|\boldsymbol{x}_r - \boldsymbol{u}\|^2 + P_u \|\boldsymbol{x}_r - \boldsymbol{b}\|^2 + \xi^{-1} \|\boldsymbol{x}_r - \boldsymbol{u}\|^2 \|\boldsymbol{x}_r - \boldsymbol{b}\|^2 \\
&= p_r^{\mathrm{U}} \|\alpha\boldsymbol{s} + \alpha_\perp \boldsymbol{s}_\perp + h\boldsymbol{e}_z\|^2 \\
&\quad + P_u \|\boldsymbol{u} + \alpha\boldsymbol{s} + \alpha_\perp \boldsymbol{s}_\perp + h\boldsymbol{e}_z - \boldsymbol{b}\|^2 \\
&\quad + \xi^{-1} \|\alpha\boldsymbol{s} + \alpha_\perp \boldsymbol{s}_\perp + h\boldsymbol{e}_z\|^2 \, \|\boldsymbol{u} + \alpha\boldsymbol{s} + \alpha_\perp \boldsymbol{s}_\perp + h\boldsymbol{e}_z - \boldsymbol{b}\|^2 \\
&= p_r^{\mathrm{U}} (\alpha^2 + \alpha_\perp^2 + h^2) + P_u ((M-\alpha)^2 + \alpha_\perp^2 + h^2) \\
&\quad + \xi^{-1} (\alpha^2 + \alpha_\perp^2 + h^2)((M-\alpha)^2 + \alpha_\perp^2 + h^2) \\
&\geq p_r^{\mathrm{U}} (\alpha^2 + h^2) + P_u ((M-\alpha)^2 + h^2) \\
&\quad + \xi^{-1} (\alpha^2 + h^2)((M-\alpha)^2 + h^2),
\end{aligned} \tag{49}$$

where $M = \|\boldsymbol{b} - \boldsymbol{u}\|$, and the last inequality is obtained by setting $\alpha_\perp = 0$. In addition, the denominator of the second logarithmic term in (14) can have a similar lower bound. Therefore, the sum rate in (14) would be maximized if $\boldsymbol{x}_r = \boldsymbol{u} + \alpha\boldsymbol{s} + h\boldsymbol{e}_z$. Besides, for $\alpha \geq M$, the optimal α that minimizes the lower bound in (49) is $\alpha = M$. So, the optimal UAV position, when projected onto the x-y plane, must be on the line segment connecting the UE and the BS. ■

Appendix B
Proof of Proposition 1

Note that

$$\begin{aligned}
&R_k^{\mathrm{D}} \left(p_{b,k}, p_{r,k}^{\mathrm{D}}, \boldsymbol{x}_r\right) \\
&= \log\left(1 + \frac{\xi^2 p_{r,k}^{\mathrm{D}} p_{b,k} d_{rb}^{-2} d_{kr}^{-2}}{\xi p_{r,k}^{\mathrm{D}} d_{kr}^{-2} + \xi p_{b,k} d_{rb}^{-2} + 1}\right) \qquad (50) \\
&= \log\left(1 + \frac{1}{\xi^{-1}\frac{\|\boldsymbol{d}_{rb}\|^2}{p_{b,k}} + \xi^{-1}\frac{\|\boldsymbol{d}_{kr}\|^2}{p_{r,k}^{\mathrm{D}}} + \xi^{-2}\frac{\|\boldsymbol{d}_{rb}\|^2}{p_{b,k}}\frac{\|\boldsymbol{d}_{kr}\|^2}{p_{r,k}^{\mathrm{D}}}}\right) \\
&= \log\left(1 + \xi^{-1}\frac{\|\boldsymbol{d}_{rb}\|^2}{p_{b,k}}\right) + \log\left(1 + \xi^{-1}\frac{\|\boldsymbol{d}_{kr}\|^2}{p_{r,k}^{\mathrm{D}}}\right) \\
&\quad - \log\left(\xi^{-1}\frac{\|\boldsymbol{d}_{rb}\|^2}{p_{b,k}} + \xi^{-1}\frac{\|\boldsymbol{d}_{kr}\|^2}{p_{r,k}^{\mathrm{D}}} + \xi^{-2}\frac{\|\boldsymbol{d}_{rb}\|^2}{p_{b,k}}\frac{\|\boldsymbol{d}_{kr}\|^2}{p_{r,k}^{\mathrm{D}}}\right). \qquad (51)
\end{aligned}$$

Since $\frac{\|\mathbf{x}\|^2}{p}$ is convex in $\mathbf{x} \in \mathbb{R}^n$ and $p > 0$, its first-order approximation at a given point $(\bar{\mathbf{x}}, \bar{p})$ is a lower bound, i.e.,

$$\frac{\|\mathbf{x}\|^2}{p} \geq \frac{2\bar{\mathbf{x}}^T}{\bar{p}}\mathbf{x} - \frac{\|\bar{\mathbf{x}}\|^2}{\bar{p}^2}p. \tag{52}$$

Given any reference point $(\bar{p}_{b,k}, \bar{p}^{\mathrm{D}}_{r,k}, \bar{\boldsymbol{x}}_r)$, the first and second terms in the right hand side (RHS) of (51) can be bounded as

$$\log\left(1+\xi^{-1}\frac{\|\boldsymbol{d}_{rb}\|^2}{p_{b,k}}\right) \geq \log\left(1+\xi^{-1}\left(\frac{2\bar{\boldsymbol{d}}_{rb}^T}{\bar{p}_{b,k}}\boldsymbol{d}_{rb}-\frac{\|\bar{\boldsymbol{d}}_{rb}\|^2}{\bar{p}_{b,k}^2}p_{b,k}\right)\right), \quad (53)$$

$$\log\left(1+\xi^{-1}\frac{\|\boldsymbol{d}_{kr}\|^2}{p^{\mathrm{D}}_{r,k}}\right) \geq \log\left(1+\xi^{-1}\left(\frac{2\bar{\boldsymbol{d}}_{kr}^T}{\bar{p}^{\mathrm{D}}_{r,k}}\boldsymbol{d}_{kr}-\frac{\|\bar{\boldsymbol{d}}_{kr}\|^2}{(\bar{p}^{\mathrm{D}}_{r,k})^2}p^{\mathrm{D}}_{r,k}\right)\right), \quad (54)$$

where both of the lower bounds are concave functions of $(p_{b,k}, p^{\mathrm{D}}_{r,k}, \boldsymbol{x}_r)$. Since $-\log(1+x)$ is convex satisfying $-\log(x) \geq -\log(\bar{x}) + \frac{\bar{x}-x}{\bar{x}}$ for $\bar{x}>0$, the third term in the RHS of (51) can be bounded as

$$\begin{aligned}&-\log\left(\xi^{-1}\frac{\|\boldsymbol{d}_{rb}\|^2}{p_{b,k}}+\xi^{-1}\frac{\|\boldsymbol{d}_{kr}\|^2}{p^{\mathrm{D}}_{r,k}}+\xi^{-2}\frac{\|\boldsymbol{d}_{rb}\|^2}{p_{b,k}}\frac{\|\boldsymbol{d}_{kr}\|^2}{p^{\mathrm{D}}_{r,k}}\right)\\ &\geq -\log(\bar{I}^{\mathrm{D}}_k)+1 -\frac{1}{\bar{I}^{\mathrm{D}}_k}\left(\xi^{-1}\frac{\|\boldsymbol{d}_{rb}\|^2}{p_{b,k}}+\xi^{-1}\frac{\|\boldsymbol{d}_{kr}\|^2}{p^{\mathrm{D}}_{r,k}}+\xi^{-2}\frac{\|\boldsymbol{d}_{rb}\|^2}{p_{b,k}}\frac{\|\boldsymbol{d}_{kr}\|^2}{p^{\mathrm{D}}_{r,k}}\right),\end{aligned} \quad (55)$$

where $\bar{I}^{\mathrm{D}}_k$ is given in (21).

By applying $xy=\frac{1}{2}(x+y)^2-\left(\frac{1}{2}x^2+\frac{1}{2}y^2\right)$, to the term $-\frac{\|\boldsymbol{d}_{rb}\|^2}{p_{b,k}}\frac{\|\boldsymbol{d}_{kr}\|^2}{p^{\mathrm{D}}_{r,k}}$ in the RHS of (55), we have

$$\begin{aligned}-\frac{\|\boldsymbol{d}_{rb}\|^2}{p_{b,k}}\frac{\|\boldsymbol{d}_{kr}\|^2}{p^{\mathrm{D}}_{r,k}} &= -\frac{1}{2}\left(\frac{\|\boldsymbol{d}_{rb}\|^2}{p_{b,k}}+\frac{\|\boldsymbol{d}_{kr}\|^2}{p^{\mathrm{D}}_{r,k}}\right)^2\\ &\quad+\frac{1}{2}\left(\frac{\|\boldsymbol{d}_{rb}\|^2}{p_{b,k}}\right)^2+\frac{1}{2}\left(\frac{\|\boldsymbol{d}_{kr}\|^2}{p^{\mathrm{D}}_{r,k}}\right)^2.\end{aligned} \quad (56)$$

In addition, by applying the first-order condition of the convex function $\frac{(\|\mathbf{x}\|^2)^2}{p^2}$, i.e.,

$$\frac{\left(\|\mathbf{x}\|^2\right)^2}{p^2} \geq \frac{4\|\bar{\mathbf{x}}\|^2\bar{\mathbf{x}}^T\mathbf{x}}{\bar{p}^2}-\frac{2(\|\bar{\mathbf{x}}\|^2)^2\ p}{\bar{p}^3}-\frac{(\|\bar{\mathbf{x}}\|^2)^2}{\bar{p}^2}, \quad (57)$$

to the last two terms in the RHS of (56), we can further obtain a lower bound of (55) as

$$\begin{aligned}&-\log\left(\xi^{-1}\frac{\|\boldsymbol{d}_{rb}\|^2}{p_{b,k}}+\xi^{-1}\frac{\|\boldsymbol{d}_{kr}\|^2}{p^{\mathrm{D}}_{r,k}}+\xi^{-2}\frac{\|\boldsymbol{d}_{rb}\|^2}{p_{b,k}}\frac{\|\boldsymbol{d}_{kr}\|^2}{p^{\mathrm{D}}_{r,k}}\right)\\ &\geq -\log(\bar{I}^{\mathrm{D}}_k)+1-\frac{1}{\bar{I}^{\mathrm{D}}_k\xi}\left(\frac{\|\boldsymbol{d}_{rb}\|^2}{p_{b,k}}+\frac{\|\boldsymbol{d}_{kr}\|^2}{p^{\mathrm{D}}_{r,k}}\right)\\ &\quad-\frac{1}{2\bar{I}^{\mathrm{D}}_k\xi^2}\left(\frac{\|\boldsymbol{d}_{rb}\|^2}{p_{b,k}}+\frac{\|\boldsymbol{d}_{kr}\|^2}{p^{\mathrm{D}}_{r,k}}\right)^2+\frac{1}{2\bar{I}^{\mathrm{D}}_k\xi^2}\\ &\quad\times\left(\left(\frac{4\|\bar{\boldsymbol{d}}_{rb}\|^2\bar{\boldsymbol{d}}_{rb}^T\boldsymbol{d}_{rb}}{\bar{p}^2_{b,k}}-\frac{2(\|\bar{\boldsymbol{d}}_{rb}\|^2)^2p_{b,k}}{\bar{p}^3_{b,k}}-\frac{(\|\bar{\boldsymbol{d}}_{rb}\|^2)^2}{\bar{p}^2_{b,k}}\right)\right.\\ &\quad\left.+\left(\frac{4\|\bar{\boldsymbol{d}}_{kr}\|^2\bar{\boldsymbol{d}}_{kr}^T\boldsymbol{d}_{kr}}{(\bar{p}^{\mathrm{D}}_{r,k})^2}-\frac{2(\|\bar{\boldsymbol{d}}_{kr}\|^2)^2p^{\mathrm{D}}_{r,k}}{(\bar{p}^{\mathrm{D}}_{r,k})^3}-\frac{(\|\bar{\boldsymbol{d}}_{rb}\|^2)^2}{(\bar{p}^{\mathrm{D}}_{r,k})^2}\right)\right).\end{aligned} \quad (58)$$

By substituting (53), (54) and (58) into (51), one then obtains (25). It is easy to check that

$$R^{\mathrm{D}}_k(\bar{\boldsymbol{x}}_r, \bar{p}_{b,k}, \bar{p}^{\mathrm{D}}_{r,k}) = \bar{R}^{\mathrm{D}}_k(\bar{\boldsymbol{x}}_r, \bar{p}_{b,k}, \bar{p}^{\mathrm{D}}_{r,k}). \quad (59)$$

Equation (26) can be derived in an analogous fashion; the details are skipped here.

■

APPENDIX C
DERIVATION OF (31) AND (32)

Let us introduce auxiliary variables $a^{\mathrm{D}}_{r,k}=\sqrt{p^{\mathrm{D}}_{r,k}}, a_{b,k}=\sqrt{p_{b,k}}, s_{kr}=d^2_{kr}$, $s_{rb}=d^2_{rb}$, and $J^{\mathrm{D}}_k=\xi(\frac{(a^{\mathrm{D}}_{r,k})^2}{s_{kr}}+\frac{a^2_{b,k}}{s_{rb}})$. Moreover, for a given feasible point $(\bar{\boldsymbol{p}}_b, \bar{\boldsymbol{p}}^{\mathrm{D}}_r, \bar{\boldsymbol{x}}_r)$, we define $\bar{a}^{\mathrm{D}}_{r,k}=\sqrt{\bar{p}^{\mathrm{D}}_{r,k}}, \bar{a}_{b,k}=\sqrt{\bar{p}_{b,k}}$, $\bar{s}_{kr}=\bar{d}^2_{kr}$, $\bar{s}_{rb}=\bar{d}^2_{rb}$, and $\bar{J}^{\mathrm{D}}_k=\xi(\frac{(\bar{a}^{\mathrm{D}}_{r,k})^2}{\bar{s}_{kr}}+\frac{\bar{a}^2_{b,k}}{\bar{s}_{rb}})$. We can bound $R^{\mathrm{D}}_k\left(p_{b,k}, p^{\mathrm{D}}_{r,k}, \boldsymbol{x}_r\right) = R^{\mathrm{D}}_k\left(a_{b,k}, a^{\mathrm{D}}_{r,k}, \boldsymbol{x}_r\right)$ as follows

$$\begin{aligned}&R^{\mathrm{D}}_k\left(a_{b,k}, a^{\mathrm{D}}_{r,k}, \boldsymbol{x}_r\right)\\ &=\log\left(1+\frac{\xi^2\frac{a^2_{b,k}(a^{\mathrm{D}}_{r,k})^2}{s_{rb}s_{kr}}}{\xi\frac{(a^{\mathrm{D}}_{r,k})^2}{s_{kr}}+\xi\frac{a^2_{b,k}}{s_{rb}}+1}\right)\\ &=\log\left(1+\xi\frac{(a^{\mathrm{D}}_{r,k})^2}{s_{kr}}+\xi\frac{a^2_{b,k}}{s_{rb}}+\xi^2\frac{a^2_{b,k}(a^{\mathrm{D}}_{r,k})^2}{s_{rb}s_{kr}}\right)\\ &\quad-\log\left(1+\xi\frac{(a^{\mathrm{D}}_{r,k})^2}{s_{kr}}+\xi\frac{a^2_{b,k}}{s_{rb}}\right)\\ &=\log\left(1+\xi\frac{(a^{\mathrm{D}}_{r,k})^2}{s_{kr}}\right)+\log\left(1+\xi\frac{a^2_{b,k}}{s_{rb}}\right)\\ &\quad-\log\left(1+\xi\frac{(a^{\mathrm{D}}_{r,k})^2}{s_{kr}}+\xi\frac{a^2_{b,k}}{s_{rb}}\right) \quad (60)\\ &\geq\log\left(1+\xi\frac{2\bar{a}^{\mathrm{D}}_{r,k}}{\bar{s}_{kr}}a^{\mathrm{D}}_{r,k}-\xi\frac{(\bar{a}^{\mathrm{D}}_{r,k})^2}{\bar{s}^2_{kr}}s_{kr}\right)\\ &\quad+\log\left(1+\xi\frac{2\bar{a}_{b,k}}{\bar{s}_{rb}}a_{b,k}-\xi\frac{(\bar{a}_{b,k})^2}{\bar{s}^2_{rb}}s_{rb}\right)-\log\left(1+\bar{J}^{\mathrm{D}}_k\right)\\ &\quad+\frac{\bar{J}^{\mathrm{D}}_k}{1+\bar{J}^{\mathrm{D}}_k}-\frac{\xi}{1+\bar{J}^{\mathrm{D}}_k}\left(\frac{(a^{\mathrm{D}}_{r,k})^2}{\|\mathbf{x}_r-\boldsymbol{u}_k\|^2}+\frac{a^2_{b,k}}{\|\mathbf{x}_r-\boldsymbol{b}\|^2}\right) \quad (61)\\ &\geq\log\left(1+\xi\frac{2\bar{a}^{\mathrm{D}}_{r,k}}{\bar{s}_{kr}}a^{\mathrm{D}}_{r,k}-\xi\frac{(\bar{a}^{\mathrm{D}}_{r,k})^2}{\bar{s}^2_{kr}}\|\mathbf{x}_r-\boldsymbol{u}_k\|^2\right)\\ &\quad+\log\left(1+\xi\frac{2\bar{a}_{b,k}}{\bar{s}_{rb}}a_{b,k}-\xi\frac{(\bar{a}_{b,k})^2}{\bar{s}^2_{rb}}\|\mathbf{x}_r-\boldsymbol{b}\|^2\right)-\log\left(1+\bar{J}^{\mathrm{D}}_k\right)\\ &\quad+\frac{\bar{J}^{\mathrm{D}}_k}{1+\bar{J}^{\mathrm{D}}_k}-\frac{\xi}{1+\bar{J}^{\mathrm{D}}_k}\left(\frac{(a^{\mathrm{D}}_{r,k})^2}{\|\boldsymbol{u}_k\|^2-\|\bar{\mathbf{x}}_r\|^2+2(\bar{\mathbf{x}}_r-\boldsymbol{u}_k)^T\mathbf{x}_r}\right.\\ &\quad\left.+\frac{a^2_{b,k}}{\|\boldsymbol{b}\|^2-\|\bar{\mathbf{x}}_r\|^2+2(\bar{\mathbf{x}}_r-\boldsymbol{b})^T\mathbf{x}_r}\right), \quad (62)\end{aligned}$$

which is the surrogate function in (31). To obtain (61), we have applied (52) to $\frac{(a^{\mathrm{D}}_{r,k})^2}{s_{kr}}$ and $\frac{a^2_{b,k}}{s_{rb}}$ in the first two logarithmic terms in (60); we have also applied the first-order Taylor lower bound of $-\log(1+x)\geq-\log(1+\bar{x})-\frac{x-\bar{x}}{1+\bar{x}}$ to the third logarithmic term in (60). The inequality in (62) is obtained

by applying the first-order Taylor lower bound to $\|\mathbf{x}_r - \boldsymbol{u}_k\|^2$ and $\|\mathbf{x}_r - \boldsymbol{b}\|^2$, respectively.

The surrogate function in (32) for $R_k^{\mathrm{U}}\left(p_{r,k}^{\mathrm{U}}, \boldsymbol{x}_r\right)$ can be obtained in a similar fashion. ■

APPENDIX D
PROOF OF PROPOSITION 2

Since $\bar{R}_k^{\mathrm{D}}$ (resp. $\hat{R}_k^{\mathrm{D}}$) and $\bar{R}_k^{\mathrm{U}}$ (resp. $\hat{R}_k^{\mathrm{U}}$) have the same structure, we only consider $\bar{R}_k^{\mathrm{D}}$ and $\hat{R}_k^{\mathrm{D}}$ in the proof. Note that $\bar{R}_k^{\mathrm{D}}$ and $\hat{R}_k^{\mathrm{D}}$ are concave functions, and thereby their Hessian matrices are negative semi-definite, i.e., $-\nabla_{\mathbf{x}_r}^2 \bar{R}_k^{\mathrm{D}}\left(\boldsymbol{x}_r, \boldsymbol{p}\right) \succeq \mathbf{0}$ and $-\nabla_{\mathbf{x}_r}^2 \hat{R}_k^{\mathrm{D}}\left(\boldsymbol{x}_r, \boldsymbol{p}\right) \succeq \mathbf{0}$.

By (25), the negative Hessian of $\bar{R}_k^{\mathrm{D}}(\boldsymbol{x}_r, \bar{\boldsymbol{p}})$ with respect to $\boldsymbol{x}_r$ can be derived as

$$
\begin{aligned}
-\nabla_{\mathbf{x}_r}^2 \bar{R}_k^{\mathrm{D}}\left(\boldsymbol{x}_r, \bar{\boldsymbol{p}}\right) &= \frac{4\bar{\boldsymbol{d}}_{rb}\bar{\boldsymbol{d}}_{rb}^T}{\left(\xi\bar{p}_{b,k} + 2\bar{\boldsymbol{d}}_{rb}^T\boldsymbol{d}_{rb} - \|\bar{\boldsymbol{d}}_{rb}\|^2\bar{p}_{b,k}\right)^2} \\
&+ \frac{4\bar{\boldsymbol{d}}_{kr}\bar{\boldsymbol{d}}_{kr}^T}{\left(\xi\bar{p}_{r,k}^{\mathrm{D}} + 2\bar{\boldsymbol{d}}_{kr}^T\boldsymbol{d}_{kr} - \|\bar{\boldsymbol{d}}_{kr}\|^2\bar{p}_{r,k}^{\mathrm{D}}\right)^2} + \frac{2}{\bar{I}_k^{\mathrm{D}}\xi}\left(\frac{1}{\bar{p}_{b,k}} + \frac{1}{\bar{p}_{r,k}^{\mathrm{D}}}\right)\boldsymbol{I} \\
&+ \frac{2}{\bar{I}_k^{\mathrm{D}}\xi^2}\Bigg(\frac{2\boldsymbol{d}_{rb}\boldsymbol{d}_{rb}^T + \|\boldsymbol{d}_{rb}\|^2\boldsymbol{I}}{\bar{p}_{b,k}^2} + \frac{2\boldsymbol{d}_{rb}\boldsymbol{d}_{kr}^T + \|\boldsymbol{d}_{rb}\|^2\boldsymbol{I}}{\bar{p}_{b,k}\bar{p}_{r,k}^{\mathrm{D}}} \\
&+ \frac{2\boldsymbol{d}_{kr}\boldsymbol{d}_{rb}^T + \|\boldsymbol{d}_{kr}\|^2\boldsymbol{I}}{\bar{p}_{r,k}^{\mathrm{D}}\bar{p}_{b,k}} + \frac{2\boldsymbol{d}_{kr}\boldsymbol{d}_{kr}^T + \|\boldsymbol{d}_{kr}\|^2\boldsymbol{I}}{(\bar{p}_{r,k}^{\mathrm{D}})^2}\Bigg),
\end{aligned} \tag{63}
$$

where $\boldsymbol{I}$ is the identity matrix and $\bar{I}_k^{\mathrm{D}}$ is given in (21) which is a function of ξ. As seen, when ξ is large, the first two terms in the right hand side (RHS) of (63) is bounded by $\mathcal{O}(\xi^{-2})\boldsymbol{I}$, the last four terms in the RHS of (63) is bounded by $\mathcal{O}(\xi^{-1})\boldsymbol{I}$, and the third term in the RHS of (63) is bounded by

$$
\begin{aligned}
\frac{2}{\bar{I}_k^{\mathrm{D}}\xi}\left(\frac{1}{\bar{p}_{b,k}} + \frac{1}{\bar{p}_{r,k}^{\mathrm{D}}}\right)\boldsymbol{I} &\preceq \frac{2}{\frac{\|\bar{\boldsymbol{d}}_{rb}\|^2}{\bar{p}_{b,k}} + \frac{\|\bar{\boldsymbol{d}}_{kr}\|^2}{\bar{p}_{r,k}^{D}}}\left(\frac{1}{\bar{p}_{b,k}} + \frac{1}{\bar{p}_{r,k}^{\mathrm{D}}}\right)\boldsymbol{I} \\
&= 2\left(\frac{\frac{\|\bar{\boldsymbol{d}}_{rb}\|^2}{\bar{p}_{b,k}} + \frac{\|\bar{\boldsymbol{d}}_{kr}\|^2}{\bar{p}_{r,k}^{D}}}{\frac{1}{\bar{p}_{b,k}} + \frac{1}{\bar{p}_{r,k}^{\mathrm{D}}}}\right)^{-1}\boldsymbol{I} \\
&\preceq \frac{2}{\min\left\{\|\bar{\boldsymbol{d}}_{rb}\|^2, \|\bar{\boldsymbol{d}}_{kr}\|^2\right\}}\boldsymbol{I}.
\end{aligned} \tag{64}
$$

Thus, the maximum eigenvalue of $-\nabla_{\mathbf{x}_r}^2 \bar{R}_k^{\mathrm{D}}\left(\boldsymbol{x}_r, \bar{\boldsymbol{p}}\right)$ is bounded as

$$
\lambda_{\max}(-\nabla_{\boldsymbol{x}_r}^2 \bar{R}_k^{\mathrm{D}}(\boldsymbol{x}_r, \bar{\boldsymbol{p}})) \leq \mathcal{O}(\xi^{-1}) + \frac{2}{\min\left\{\|\bar{\boldsymbol{d}}_{rb}\|^2, \|\bar{\boldsymbol{d}}_{kr}\|^2\right\}}. \tag{65}
$$

By (31), the negative Hessian matrix of $\hat{R}_k^{\mathrm{D}}\left(\boldsymbol{x}_r, \bar{\boldsymbol{p}}\right)$ w.r.t. $\boldsymbol{x}_r$ is

$$
\begin{aligned}
-\nabla_{\mathbf{x}_r}^2 \hat{R}_k^{\mathrm{D}}\left(\boldsymbol{x}_r, \bar{\boldsymbol{p}}\right) &= \frac{4}{\left(\frac{\|\bar{\boldsymbol{d}}_{rb}\|^4}{\xi\bar{p}_{b,k}} + 2\|\bar{\boldsymbol{d}}_{rb}\|^2 - \|\boldsymbol{d}_{rb}\|^2\right)^2}\boldsymbol{d}_{rb}\boldsymbol{d}_{rb}^T \\
&+ \frac{2}{\frac{\|\bar{\boldsymbol{d}}_{rb}\|^4}{\xi\bar{p}_{b,k}} + 2\|\bar{\boldsymbol{d}}_{rb}\|^2 - \|\boldsymbol{d}_{rb}\|^2}\boldsymbol{I} \\
&+ \frac{\xi}{1 + \bar{J}_k^{\mathrm{D}}}\frac{8p_{b,k}\bar{\boldsymbol{d}}_{rb}\bar{\boldsymbol{d}}_{rb}^T}{\left(2\bar{\boldsymbol{d}}_{rb}^T\boldsymbol{d}_{rb} - \|\bar{\boldsymbol{d}}_{rb}\|^2\right)^3} \\
&+ \frac{4}{\left(\frac{\|\bar{\boldsymbol{d}}_{kr}\|^4}{\xi\bar{p}_{r,k}^{\mathrm{D}}} + 2\|\bar{\boldsymbol{d}}_{kr}\|^2 - \|\boldsymbol{d}_{kr}\|^2\right)^2}\boldsymbol{d}_{kr}\boldsymbol{d}_{kr}^T \\
&+ \frac{2}{\frac{\|\bar{\boldsymbol{d}}_{kr}\|^4}{\xi\bar{p}_{r,k}^{\mathrm{D}}} + 2\|\bar{\boldsymbol{d}}_{kr}\|^2 - \|\boldsymbol{d}_{kr}\|^2}\boldsymbol{I} \\
&+ \frac{\xi}{1 + \bar{J}_k^{\mathrm{D}}}\frac{8p_{r,k}^{\mathrm{D}}\bar{\boldsymbol{d}}_{kr}\bar{\boldsymbol{d}}_{kr}^T}{\left(2\bar{\boldsymbol{d}}_{kr}^T\boldsymbol{d}_{kr} - \|\bar{\boldsymbol{d}}_{kr}\|^2\right)^3},
\end{aligned} \tag{66}
$$

where $\bar{J}_k^{\mathrm{D}}$ is given in (33). One can see that each term in the RHS of (66) is bounded by $\mathcal{O}(1)$ when ξ is large. Thus,

$$
\lambda_{\max}(-\nabla_{\boldsymbol{x}_r}^2 \hat{R}_k^{\mathrm{D}}(\boldsymbol{x}_r, \bar{\boldsymbol{p}})) \leq \mathcal{O}(1). \tag{67}
$$

To show (36), let $\boldsymbol{x}_r = \bar{\boldsymbol{x}}_r$ in (66) and take $\xi \to \infty$. We then obtain

$$
\begin{aligned}
&\lim_{\xi\to\infty} -\nabla_{\mathbf{x}_r}^2 \hat{R}_k^{\mathrm{D}}\left(\bar{\boldsymbol{x}}_r, \bar{\boldsymbol{p}}\right) \\
&= \frac{4}{\|\bar{\boldsymbol{d}}_{rb}\|^6}\bar{\boldsymbol{d}}_{rb}\bar{\boldsymbol{d}}_{rb}^T + \frac{2}{\|\bar{\boldsymbol{d}}_{rb}\|^2}\boldsymbol{I} \\
&\quad + \frac{1}{\frac{\bar{p}_{r,k}^{\mathrm{D}}}{\|\bar{\boldsymbol{d}}_{kr}\|^2} + \frac{\bar{p}_{b,k}}{\|\bar{\boldsymbol{d}}_{rb}\|^2}}\frac{8\bar{p}_{b,k}}{\|\bar{\boldsymbol{d}}_{rb}\|^6}\bar{\boldsymbol{d}}_{rb}\bar{\boldsymbol{d}}_{rb}^T + \frac{4}{\|\bar{\boldsymbol{d}}_{kr}\|^4}\bar{\boldsymbol{d}}_{kr}\bar{\boldsymbol{d}}_{kr}^T \\
&\quad + \frac{2}{\|\bar{\boldsymbol{d}}_{kr}\|^2}\boldsymbol{I} + \frac{1}{\frac{\bar{p}_{r,k}^{\mathrm{D}}}{\|\bar{\boldsymbol{d}}_{kr}\|^2} + \frac{\bar{p}_{b,k}}{\|\bar{\boldsymbol{d}}_{rb}\|^2}}\frac{8\bar{p}_{r,k}^{\mathrm{D}}}{\|\bar{\boldsymbol{d}}_{kr}\|^6}\bar{\boldsymbol{d}}_{kr}\bar{\boldsymbol{d}}_{kr}^T \\
&\quad \succ \frac{2}{\|\bar{\boldsymbol{d}}_{rb}\|^2}\boldsymbol{I} + \frac{2}{\|\bar{\boldsymbol{d}}_{kr}\|^2}\boldsymbol{I} \succ \frac{2}{\min\left\{\|\bar{\boldsymbol{d}}_{rb}\|^2, \|\bar{\boldsymbol{d}}_{kr}\|^2\right\}}\boldsymbol{I}.
\end{aligned} \tag{68}
$$

From the above lower bound and (65), we conclude that, when $\xi \to \infty$,

$$
\begin{aligned}
\lambda_{\max}(-\nabla_{\boldsymbol{x}_r}^2 \hat{R}_k^{\mathrm{D}}(\bar{\boldsymbol{x}}_r, \bar{\boldsymbol{p}})) &\geq \lambda_{\min}(-\nabla_{\boldsymbol{x}_r}^2 \hat{R}_k^{\mathrm{D}}(\bar{\boldsymbol{x}}_r, \bar{\boldsymbol{p}})) \\
&> \lambda_{\max}(-\nabla_{\boldsymbol{x}_r}^2 \bar{R}_k^{\mathrm{D}}(\bar{\boldsymbol{x}}_r, \bar{\boldsymbol{p}})).
\end{aligned} \tag{69}
$$

The proof is complete. ■

REFERENCES

[1] Y. Zeng, R. Zhang, and T. J. Lim, "Wireless communications with unmanned aerial vehicles: Opportunities and challenges," *IEEE Commun. Mag.*, vol. 54, no. 5, pp. 36–42, May 2016.

[2] M. Mozaffari, W. Saad, M. Bennis, Y.-H. Nam, and M. Debbah, "A tutorial on UAVs for wireless networks: Applications, challenges, and open problems," *IEEE Commun. Surveys Tuts.*, vol. 21, no. 3, pp. 2334–2360, 3rd Quart., 2019.

[3] Y. Zeng, Q. Wu, and R. Zhang, "Accessing from the sky: A tutorial on UAV communications for 5G and beyond," Mar. 2019, *arXiv:1903.05289*. [Online]. Available: https://arxiv.org/abs/1903.05289

[4] Qualcomm. *Paving the Path to 5G: Optimizing Commercial LTE Networks for Drone Communication*. Acceseed: Sep. 6, 2016. [Online]. Available: https://www.qualcomm.com/news/onq/2016/09/06/paving-path-5goptimizing-commercial-lte-networks-drone-communication

[5] R. Sun, "Dual-band non-stationary channel modeling for the air-ground channel," Ph.D. dissertation, Dept. Elect. Eng., Univ. South Carolina, Columbia, SC, USA, Jul. 2015.

[6] Y. Zeng and R. Zhang, "Energy-efficient UAV communication with trajectory optimization," *IEEE Trans. Wireless Commun.*, vol. 16, no. 6, pp. 3747–3760, Jun. 2017.

[7] Q. Wu and R. Zhang, "Common throughput maximization in UAV-enabled OFDMA systems with delay consideration," *IEEE Trans. Commun.*, vol. 66, no. 12, pp. 6614–6627, Dec. 2018.

[8] H. He, S. Zhang, Y. Zeng, and R. Zhang, "Joint altitude and beamwidth optimization for UAV-enabled multiuser communications," *IEEE Commun. Lett.*, vol. 22, no. 2, pp. 344–347, Feb. 2018.

[9] J. Lyu, Y. Zeng, R. Zhang, and T. J. Lim, "Placement optimization of UAV-mounted mobile base stations," *IEEE Commun. Lett.*, vol. 21, no. 3, pp. 604–607, Mar. 2017.

[10] Q. Wu, Y. Zeng, and R. Zhang, "Joint trajectory and communication design for multi-UAV enabled wireless networks," *IEEE Trans. Wireless Commun.*, vol. 17, no. 3, pp. 2109–2121, Mar. 2018.

[11] C. Zhang and W. Zhang, "Spectrum sharing for drone networks," *IEEE J. Sel. Areas Commun.*, vol. 35, no. 1, pp. 136–144, Jan. 2017.

[12] E. Larsen, L. Landmark, and Ø. Kure, "Optimal UAV relay positions in multi-rate networks," in *Proc. Wireless Days*, Mar. 2017, pp. 8–14.

[13] P. Zhan, K. Yu, and A. L. Swindlehurst, "Wireless relay communications with unmanned aerial vehicles: Performance and optimization," *IEEE Trans. Aerosp. Electron. Syst.*, vol. 47, no. 3, pp. 2068–2085, Jul. 2011.

[14] Y. Zeng, R. Zhang, and T. J. Lim, "Throughput maximization for uav-enabled mobile relaying systems," *IEEE Trans. Commun.*, vol. 64, no. 12, pp. 4983–4996, Dec. 2016.

[15] L. Liu, S. Zhang, and R. Zhang, "CoMP in the sky: UAV placement and movement optimization for multi-user communications," *IEEE Trans. Commun.*, vol. 67, no. 8, pp. 5645–5658, Aug. 2019.

[16] J. Chen and D. Gesbert, "Local map-assisted positioning for flying wireless relays," Jan. 2018, *arXiv:1801.03595*. [Online]. Available: https://arxiv.org/abs/1801.03595

[17] M. Horiuchi, H. Nishiyama, N. Kato, F. Ono, and R. Miura, "Throughput maximization for long-distance real-time data transmission over multiple UAVs," in *Proc. IEEE ICC*, Kuala Lumpur, Malaysia, May 2016, pp. 1–6.

[18] Z. Han, A. L. Swindlehurst, and K. J. R. Liu, "Optimization of MANET connectivity via smart deployment/movement of unmanned air vehicles," *IEEE Trans. Veh. Technol.*, vol. 58, no. 7, pp. 3533–3546, Sep. 2009.

[19] A. Chattopadhyay, A. Ghosh, and A. Kumar, "Asynchronous stochastic approximation based learning algorithms for as-you-go deployment of wireless relay networks along a line," *IEEE Trans. Mobile Comput.*, vol. 17, no. 5, pp. 1004–1018, May 2018.

[20] M. Dong, K. Ota, M. Lin, Z. Tang, S. Du, and H. Zhu, "UAV-assisted data gathering in wireless sensor networks," *J. Supercomput.*, vol. 70, no. 3, pp. 1142–1155, Dec. 2014.

[21] F. Jiang and A. L. Swindlehurst, "Optimization of UAV heading for the ground-to-air uplink," *IEEE J. Sel. Areas Commun.*, vol. 30, no. 5, pp. 993–1005, Jun. 2012.

[22] A. E. A. A. Abdulla, Z. M. Fadlullah, H. Nishiyama, N. Kato, F. Ono, and R. Miura, "An optimal data collection technique for improved utility in UAS-aided networks," in *Proc. IEEE INFOCOM*, Toronto, ON, Canada, Apr. 2014, pp. 736–744.

[23] J. Gong, T.-H. Chang, C. Shen, and X. Chen, "Flight time minimization of UAV for data collection over wireless sensor networks," *IEEE J. Sel. Areas Commun.*, vol. 36, no. 9, pp. 1942–1954, Sep. 2018.

[24] C. Shen, T.-H. Chang, J. Gong, Y. Zeng, and R. Zhang, "Multi-UAV interference coordination via joint trajectory and power control," Sep. 2018, *arXiv:1809.05697*. [Online]. Available: https://arxiv.org/pdf/1809.05697.pdf

[25] Facebook. (2014). *Connecting the World from the Sky*. [Online]. Available: https://fbnewsroomus.files.wordpress.com/2014/03/connecting-the-world-from-the-sky1.pdf

[26] M. Mozaffari, W. Saad, M. Bennis, and M. Debbah, "Drone small cells in the clouds: Design, deployment and performance analysis," in *Proc. IEEE GLOBECOM*, San Diego, CA, USA, Dec. 2015, pp. 1–6.

[27] A. Al-Hourani, S. Kandeepan, and S. Lardner, "Optimal LAP altitude for maximum coverage," *IEEE Wireless Commun. Lett.*, vol. 3, no. 6, pp. 569–572, Dec. 2014.

[28] X. Jiang, Z. Wu, Z. Yin, and Z. Yang, "Power and trajectory optimization for UAV-enabled amplify-and-forward relay networks," *IEEE Access*, vol. 6, pp. 48688–48696, 2018.

[29] X. Jiang, Z. Wu, Z. Yin, and Z. Yang, "Joint power and trajectory design for UAV-relayed wireless systems," *IEEE Wireless Commun. Lett.*, vol. 8, no. 3, pp. 697–700, Jun. 2019.

[30] B. R. Marks and G. P. Wright, "A general inner approximation algorithm for nonconvex mathematical programs," *Oper. Res.*, vol. 26, no. 4, pp. 681–683, 1978.

[31] M. Razaviyayn, M. Hong, Z.-Q. Luo, and J.-S. Pang, "Parallel successive convex approximation for nonsmooth nonconvex optimization," in *Proc. NIPS*, Montreal, QC, Canada, 2014, pp. 1440–1448.

[32] M. Shao, Q. Li, W.-K. Ma, and A. M.-C. So, "A framework for one-bit and constant-envelope precoding over multiuser massive MISO channels," *IEEE Trans. Signal Process.*, vol. 67, no. 20, pp. 5309–5324, Oct. 2019.

[33] A. Beck and M. Teboulle, "A fast iterative shrinkage-thresholding algorithm for linear inverse problems," *SIAM J. Imag. Sci.*, vol. 2, no. 1, pp. 183–202, 2009.

[34] *Technical Specification Group Radio Access Network: Study on Enhanced LTE Support for Aerial Vehicles, 3rd Generation Partnership Project (3GPP), Version 15.0.0*, document TR 36.777, Dec. 2017.

[35] J. A. Kakar, "UAV communications: Spectral requirements, MAV and SUAV channel modeling, OFDM waveform parameters, performance and spectrum management," M.S. thesis, Bradley Dept. Elect. Comput. Eng., Virginia Tech., Blacksburg, VA, USA, 2015.

[36] *Examples of Technical Characteristics for Unmanned Aircraft Control and Non-payload Communications Links, Telecommunication Union*, document ITU-R 837-6, Nov. 2011.

[37] C. Shen, W.-C. Li, and T.-H. Chang, "Wireless information and energy transfer in multi-antenna interference channel," *IEEE Trans. Signal Process.*, vol. 62, no. 23, pp. 6249–6264, Dec. 2014.

[38] M. Razaviyayn, M. Hong, and Z.-Q. Luo, "A unified convergence analysis of block successive minimization methods for nonsmooth optimization," *SIAM J. Optim.*, vol. 23, no. 2, pp. 1126–1153, Jun. 2013.

[39] M. Hong, T.-H. Chang, X. Wang, M. Razaviyayn, S. Ma, and Z.-Q. Luo, "A block successive upper bound minimization method of multipliers for linearly constrained convex optimization," 2014, *arXiv:1401.7079*. [Online]. Available: https://arxiv.org/abs/1401.7079

[40] M. Grant and S. Boyd. (Jun. 2009). *CVX: MATLAB Software for Disciplined Convex Programming*. [Online]. Available: http://stanford.edu/boyd/cvx

[41] S. Boyd and A. Mutapcic. *Subgradient Methods*. [Online]. Available: https://www.stanford.edu/class/ee392o/

[42] D. P. Bertsekas, *Nonlinear Programming*, 2nd ed. Belmont, MA, USA: Athena Scientific, 1999.

[43] Z. Wei, X. Zhu, S. Sun, Y. Huang, L. Dong, and Y. Jiang, "Full-duplex versus half-duplex amplify-and-forward relaying: Which is more energy efficient in 60-GHz dual-hop indoor wireless systems?" *IEEE J. Sel. Areas Commun.*, vol. 33, no. 12, pp. 2936–2947, Dec. 2015.

Lei Li received the B.E. degree from Beijing Jiaotong University, Beijing, China, in 2014, and the M.S. degree from the Beijing Institute of Technology, Beijing, in 2017, all in communication engineering. He is currently pursuing the Ph.D. degree with the Bradley Department of Electrical and Computer Engineering, Virginia Polytechnic Institute and State University, Blacksburg, VA, USA. In 2018, he visited The Chinese University of Hong Kong, Shenzhen, China. His research interests include optimization and its applications in wireless communications and signal processing.

Tsung-Hui Chang (S'07–M'08–SM'17) received the B.S. degree in electrical engineering and the Ph.D. degree in communications engineering from National Tsing Hua University (NTHU), Hsinchu, Taiwan, in 2003 and 2008, respectively.

He was a Faculty Member with the Department of Electronic and Computer Engineering, National Taiwan University of Science and Technology (NTUST), from August 2012 to July 2015, a Post-Doctoral Researcher with NTHU from September 2008 to August 2011, and with the University of California at Davis, Davis, USA, from September 2011 to July 2012. He is currently an Associate Professor with the School of Science and Engineering, The Chinese University of Hong Kong, Shenzhen, China. His research interests include signal processing and optimization methods with applications to wireless communications, machine learning, and big data analysis. He received the Young Scholar Research Award from NTUST in 2014, the IEEE Communication Society Asia–Pacific Outstanding Young Researcher Award in 2015, and the IEEE Signal Processing Society Best Paper Award in 2018. From 2015 to 2018, he served as an Associate Editor for the IEEE TRANSACTIONS ON SIGNAL PROCESSING and the IEEE TRANSACTIONS ON SIGNAL AND INFORMATION PROCESSING OVER NETWORKS.

Shu Cai received the B.Sc. degree from the Hefei University of Technology, Hefei, China, in 2006, and the Ph.D. degree from Xidian University, Xi'an, China, in 2013, all in communications engineering. During his Ph.D. study, he visited Prof. Z.-Q. (Tom) Luo at the University of Minnesota Twin Cities, Minneapolis–Saint Paul, MN, USA, from 2011 to 2012. After his graduation, he joined the Nanjing University of Posts and Telecommunications, Nanjing, China, in August 2013, where he is currently an Associate Professor. His main research interests include array signal processing and signal processing for communications.